# Uncertainty and sensitivity analysis for spatial and spectral processing of Pb isotopes in zircon by atom probe tomography

# T. B. Blum<sup>1</sup>, D. A. Reinhard<sup>2</sup>, Y. Chen<sup>2</sup>, T. J. Prosa<sup>2</sup>, D. J. Larson<sup>2</sup>, and J. W. Valley<sup>1</sup>

<sup>1</sup>Department of Geoscience, University of Wisconsin – Madison, Madison, WI, 53706 USA. <sup>2</sup>CAMECA Inc., Madison WI, 53711 USA.

Corresponding author: Tyler B. Blum (tbblum@geology.wisc.edu)

# **Key Points:**

- Investigate the effect of spatial and spectral analysis of atom probe data on nanoscale geochronology
- Present systematic method for ranging and uncertainty analysis for Pb isotopes within zircon
- Lead-rich domains within zircon from Beartooth Mountains, USA correlate with 2.8 Ga thermal episode.

#### **Abstract**

Measuring <sup>207</sup>Pb/<sup>206</sup>Pb ratios by atom probe tomography (APT) has provided new insight into the nanoscale behavior of trace components in zircon, and their relationship to time, temperature and structure. Here, we analyze three APT data sets for a 3.77 Ga zircon from the Beartooth Mountains, USA, and apply systematic ranging approaches to understand the spatial and spectral uncertainties inherent in <sup>207</sup>Pb/<sup>206</sup>Pb analysis by APT. This zircon possesses two, 100% concordant U-Pb analyses by secondary ion mass spectrometry (SIMS), indicative of closed U-Pb systematics on the micron scale since crystallization. APT data sets contain subspherical Pb-rich (>0.25% atomic) domains with diameter <15 nm. Broadly consistent Pb-rich regions are defined in applying six different permutations of the two most common cluster identification algorithms. Measured <sup>207</sup>Pb/<sup>206</sup>Pb ratios within Pb-rich domains vary between  $0.794\pm0.15~(\pm2\sigma)$  and  $0.715\pm0.052$  depending on the ranging approach, cluster definition protocol and number of clusters interrogated. For the bulk APT data sets, <sup>207</sup>Pb/<sup>206</sup>Pb =  $0.353\pm0.18$ ; this is indistinguishable from the bulk  $^{207}$ Pb/ $^{206}$ Pb ratio by SIMS (0.367 $\pm0.0037$ ). and statistically distinct from the <sup>207</sup>Pb/<sup>206</sup>Pb ratio within clusters. Bulk and clustered <sup>207</sup>Pb/<sup>206</sup>Pb ratios are consistent with Pb clustering at ~2.8 Ga, during protracted metamorphism and magmatism in the Beartooth Mountains.

#### 1 Introduction

Zircon is heavily utilized in understanding earth systems and their evolution through time. The chemical and physical resistance of zircon, and its slow diffusion for most major and trace components [e.g., *Cherniak and Watson*, 2003], allows zircon to contribute to numerous studies of the silicate Earth, from detailed calibration of stratigraphic relations and the geological time scale [e.g., *Bowring and Schmitz*, 2003], to tracing of magmatic processes [e.g., *Schoene* et al., 2012], to secular trends in Earth's evolution [e.g., *Valley* et al., 2005], to provenance and the sedimentary record [e.g., *Fedo* et al., 2003]. Zircon chemistry remains one of the few means to directly study the earliest portions of Earth's history [e.g., *Cavosie* et al., 2006] and the Moon [e.g., *Nemchin* et al., 2009; *Valley* et al., 2014b]. The ability to identify the chemical manifestations of structural modification are a means to better understand controls on open system chemical behavior, as well as the timing and length scales of element mobility.

The study of zircon chemistry is intimately related to nanoscale phenomenon; a zircon's trace element and isotope chemistry, as well as its physical and chemical properties, are related to the atomistic processes of crystal growth, crystal deformation, radiation damage, structural recovery and diffusion. *Crystalline* zircon possesses slow diffusion and offers a robust record of primary chemistry; however, open system behavior of zircon components is well documented, and is most often linked to the accumulation of structural damage due to self-irradiation. Trace amounts of U and Th are incorporated into the zircon during crystallization and alpha decay events within the  $^{238}\text{U} \rightarrow ^{206}\text{Pb}$ ,  $^{235}\text{U} \rightarrow ^{207}\text{Pb}$ , and  $^{232}\text{Th} \rightarrow ^{208}\text{Pb}$  decay chains disrupt the zircon crystal structure on the nanoscale. The energetic daughter nuclei generate 5-10 nm damage domains comprised of an amorphous core which grades radially to defect rich, strained then unstrained zircon [*Ewing* et al., 2003]. If damage domains are not annealed, they become more numerous and eventually overlap to form a connected network at the "first percolation point." The accumulation of damage from this self-irradiation causes a macroscopic increase in volume, micro-fracturing, as well as a reduction in clarity, birefringence, and durability. At the atomic scale, reaction and diffusion kinetics are orders of magnitude faster for damaged zircon relative

to pristine zircon [Cherniak et al., 1991]. As a result, zircon which reaches the first percolation point is far more likely to exhibit open system chemical behavior and may possess disturbed or unreliable age and chemical systematics. Structural reconstitution acts to re-form the crystal structure where it has been damaged by alpha recoil events; however, the number, energetics, and damage state dependencies of annealing mechanisms are poorly understood [e.g. Ewing et al., 2003]. As a result, the importance of annealing at low temperature (<300°C), the relative rates of trace element diffusion and structural reconstitution, and their influence on trace element and isotope distributions remain poorly resolved. Ultimately, zircon durability and the mobility of major and trace components are functions of a zircon's nanoscale structure, and a thorough understanding of a zircons structural evolution contributes to the robust interpretation of associated geochemical information.

Atom probe tomography (APT) possesses a unique combination of spatial resolution and chemical sensitivity that is well-suited to explore the geochemical and isotopic evolution of zircon at the nanoscale. APT combines projection type microscopy with time-of-flight mass spectrometry to generate three-dimensional compositional maps with near-atomic scale resolution [Larson et al., 2013]. A needle-shaped specimen with an end tip radius on the order of 50-100 nm is held at high voltage while constituent atoms are field evaporated though application of a timed voltage pulse (for conductive materials), or laser pulse (for semiconductors and insulators). Evaporated ions are accelerated by the local electric field near the tip surface, which varies systematically across the specimen. A position sensitive detector records both the position of incident ions in detector space, as well as their time of incidence. Chemical information can be extracted from an ion's time-of-flight (which is related to the ion's mass-to-charge state ratio) while the spatial coordinates of individual ions are reconstructed based on their incident position on the detector, and specimen geometry [Gault et al., 2012; Larson et al., 2013]. The current generation of atom probe instrumentation possesses subnanometer spatial resolution, with typical mass resolving powers up to 1100 for inverted FWHM  $(M/\Delta M)$ , and detection limits down to 10 parts per million atomic (ppma) [Larson et al., 2013]. These capabilities allow the three-dimensional characterization of zircon trace element and isotope chemistry on the scale of crystal deformation, radiation damage and annealing processes. Atom probe studies of ancient zircons have revealed heterogeneous distributions of several trace components, including Y, Yb, Dy, Lu and radiogenic Pb, on the scale of 10's of nanometers. The morphology and chemistry of these domains is varied, and multiple structural/mechanistic controls on trace element re-distribution have been proposed, including diffusion to alpha-recoil damage domains [Valley et al., 2014, 2015], and partitioning/trapping by defect structures within deformed and/or reconstituted zircon [Reddy et al., 2016; Peterman et al., 2016; Piazolo et al.,2016]. The number of time, temperature, and structural histories that lead to cluster formation remains poorly constrained; however, studies that have reported Pb isotope ratios within clusters, and conclude that (1) the clustered Pb is of radiogenic origin and thus the clusters are not primary features associated with initial zircon crystallization, and (2) Pb isotope ratios both inside and outside of enriched domains can in certain cases be linked (either directly or indirectly) to the timing of nanoscale element mobility and cluster formation. In cases where cluster formation is related to a discrete, short-lived episode, the ability to measure <sup>207</sup>Pb/<sup>206</sup>Pb isotope ratios at the nanoscale can provide quantitative information regarding the timing of element redistribution. With certain assumptions, this can be used as a novel geochronometer to understand the cryptic deformation or thermal history of submicron zircon domains.

Applying this broadly to resolve episodes of element migration on the nanoscale requires both (1) characterizing the uncertainties inherent in the measurement of Pb isotopes by APT, and (2) understanding the approximations and simplifications inherent in modeling cluster ages. This contribution utilizes correlative electron backscatter diffraction (EBSD), secondary ion mass spectrometry (SIMS) and APT in a 3.77 Ga zircon from the Beartooth Mountains, Montana, to (1) provide an assessment of uncertainties in spectral analysis of Pb isotopes in APT data (especially for clusters/regions enriched in Pb and with higher signal-to-noise) and (2) evaluate how cluster identification can influence measured isotope ratios. These results provide a basis for assessing *analytical* limits of interpretation originating from measurement of <sup>207</sup>Pb/<sup>206</sup>Pb ratios within APT data.

# 1.1 Spatial and spectral uncertainties in Pb/Pb ratios by APT

An atom probe data set consists of a point cloud of ion positions and identities; construction (and subsequent analysis) of these data involve two distinct, but interacting, data types. One is an ion's time-of-flight, which is transformed into a mass-to-charge state ratio and forms the basis for affixing a user-defined ion identity. The second are the ion's XY-position (in detector space) and the evaporation sequence which are used to reconstruct an ion's xyz-position in specimen space. Uncertainties associated with one or both of these data types are not necessarily straightforward to calculate, or to propagate. There remain no community-wide "standard" analysis procedures due to in large part to (1) unique spectral and spatial complexities associated with different materials and/or material structures, and (2) the need to maintain flexibility in prioritizing spatial vs. spectral aspects of APT data sets (i.e., given the unique combination of data types in APT, different scientific questions of interest can be more appropriately answered using different permutations on data reduction). This work does not treat the general complexities of spatial and spectral analysis by APT, but focuses on those aspects of data analysis which contribute to uncertainty in measurement of Pb isotopes in zircon. This provides a general framework to assess the statistical significance of different Pb isotope ratios measured in different sub-volumes of a given data set.

Ranging (i.e., identification of peaks and placement of peak integration bounds) of APT mass spectra is a critical component of both compositional analysis and the generation of accurate atom probe reconstructions. As described elsewhere, accurate and precise ranging of peaks within the mass spectrum aims to include the entire signal, while not degrading precision by including extraneous background [e.g., *Gedcke*, 2001; *Larson* et al., 2013]. While qualitatively simple, ranging approaches vary in their ability to reproduce specimen composition [e.g., *Hudson* et al., 2011], and development of ranging protocols that yield stoichiometric compositions for any given material (particularly complex oxides) remains an active area of research [e.g., *Oberdorfer* et al., 2007; *Vella* et al., 2011; *Kirchhofer* et al., 2013]. These considerations are particularly relevant to assessing the accuracy and precision of *absolute* concentrations for major and trace components (including Pb) within zircon by APT. Importantly, both characterizing the spatial distribution of trace components, and measuring isotope ratios, are based on the *relative* concentrations, and thus can be considered independently of the more general uncertainties in compositional analysis by APT.

Lead isotope ratios are calculated through identification and ranging of <sup>207</sup>Pb and <sup>206</sup>Pb isotopes within the APT mass spectrum. Lead is a trace component in bulk zircon, and thus low total counts and significant noise mean the systematic application of "standard" ranging practices (e.g., defining range bounds at full width at one-tenth maximum, full width at one-hundredth

maximum, etc.) can be both difficult to apply rigorously and sensitive to variables such as spectral bin width. No study has systematically interrogated the dependence of <sup>207</sup>Pb/<sup>206</sup>Pb ratios (measured by APT) on spectral binning, placement of range bounds, and counting statistics, and we provide a framework for Pb isotope analysis through assessment of reproducibility and scatter in <sup>207</sup>Pb/<sup>206</sup>Pb ratios for a series of ranging approaches and spectral binning.

In addition to the uncertainties in Pb isotope ratios originating from spectral analysis, spatial aspects of data can also influence observed Pb isotope ratios. Measuring Pb signals within distinct domains of an APT data set requires defining domain boundaries; even in ideal data with no background or spatial uncertainty, different boundary definitions/thresholds will isolate distinct spatial subsets of the data. The morphology (size, shape, etc.) and composition of domains can be sensitive to these aspects of data reduction, particularly in cases where they are defined based on dilute components or components having significant gradients in composition [e.g., Valley et al., 2014]. In APT, this situation is further complicated by both spatial uncertainty inherent in reconstructing ion positions, and the fact that while background levels can be quantified *spectrally*, it is not currently possible to uniquely identify background counts spatially. All these factors manifest as uncertainty in the uniqueness and characteristics of "compositionally distinct domains" (their size, shape, number, average composition, etc.), and have implications for the measurement and interpretation of Pb isotope ratios at the nanoscale. The general treatment of uncertainty in compositional analysis due to spatial aspects of data analysis is complex, and is beyond the scope of this contribution. We treat this aspect of analysis empirically, by isolating domains based on several permutations of two common cluster analysis algorithms to look for first-order differences that may influence geological interpretation of the data.

#### 1.2 Cluster Age Modeling

Extracting temporal information from spatially heterogeneous Pb isotope ratios requires modeling of the zircon U-Pb system through time;  $^{207}$ Pb/ $^{206}$ Pb ratios alone are non-unique and require assumptions and/or boundary conditions in order to interpret their geological significance. We follow the general model of *Valley* et al. [2015], and calculate the timing of element mobility assuming clustering of radiogenic Pb produced between the time of zircon crystallization ( $t_{xln}$ , in years before present) and a discrete clustering episode in the zircon's history ( $t_2$ ). This simple model is applicable to well-behaved systems with U-Pb systematics that can be related between the micron and nanoscale. Assuming no open system behavior at the scale of observation, and vanishingly small initial Pb, the radiogenic  $^{207}$ Pb/ $^{206}$ Pb ratio for the bulk specimen at any time  $t_2$  is given by:

$$\left(\frac{^{207}Pb}{^{206}Pb}\right)^* = \left(\frac{^{235}U}{^{238}U}\right)_{xln} \left(\frac{1 - \exp(-\lambda_{235}(t_{xln} - t_2))}{1 - \exp(-\lambda_{238}(t_{xln} - t_2))}\right)$$
(1)

where  $(t_{\text{xln}}-t_2)$  represents the time elapsed since crystallization,  $\lambda_{235}$  and  $\lambda_{238}$  are the <sup>235</sup>U and <sup>238</sup>U decay constants respectively, and the (\*) denotes radiogenic Pb. If all radiogenic Pb present at time  $t_2$  migrates into a cluster volume fraction,  $f_c$ , the concentration of (<sup>207</sup>Pb\*+<sup>206</sup>Pb\*) within the clusters becomes:

$$Pb_{t2}^{*\prime} = f_c^{-1} \left[ {}^{235}U(1 - \exp(-\lambda_{235}(t_{xln} - t_2))) + {}^{238}U(1 - \exp(-\lambda_{238}(t_{xln} - t_2))) \right]$$
(2)  
$$\left( {}^{207}Pb_{206}pb_{b}} \right)_{t2}^{*\prime} = \left( {}^{207}Pb_{206}p_{b}} \right)^{*} = \left( {}^{235}U_{238}U_{xln} \left( {}^{1 - \exp(-\lambda_{235}(t_{xln} - t_2))} \right) - {}^{238}U_{xln} \left( {}^{235}U_{xln} - {}^{235}U_{xln} - {}^{235}U_{xln} - {}^{235}U_{xln} \right) \right)$$
(3)

Where (') indicates Pb within clusters. If one assumes a homogeneous ingrowth of radiogenic Pb between  $t_2$  and the present, and no element migration occurred between  $t_2$  and the present, the present day isotope ratio in clusters becomes a simple mixture of clustered Pb\* at  $t_2$  and Pb\* accrued since:

$$Pb_{T}^{*\prime} = Pb_{t2}^{*\prime} + \left[^{235}U(1 - \exp(-\lambda_{235}(t_{2}))) + {}^{238}U(1 - \exp(-\lambda_{238}(t_{2})))\right]$$

$$X_{t2}^{\prime} = \frac{Pb_{t2}^{\prime}}{Pb_{T}^{\prime}}$$

$$\left(\frac{^{207}Pb}{^{206}Pb}\right)_{P}^{*\prime} = X_{t2}^{\prime} \left(\frac{^{207}Pb}{^{206}Pb}\right)_{t2}^{*\prime} + (1 - X_{t2}^{\prime}) \left(\frac{^{235}U}{^{238}U}\right)_{t2} \left(\frac{1 - \exp(-\lambda_{235}(t_{2}))}{1 - \exp(-\lambda_{238}(t_{2}))}\right)$$

$$(6)$$

The observed ratio within clusters is thus (at its simplest) a function of zircon crystallization age, the volume fraction of clusters, and the timing of cluster formation. If the initial concentration of Pb is negligible, and the ingrowth of Pb\* between  $t_2$  and present is sufficiently dilute relative to  $Pb'_{t2}$  (i.e.,  $X'_{t2} \rightarrow 1$ ), then eqn. (3) may be used to calculate the timing of cluster formation. Additional complexity can be incorporated into this isotope model by varying: (1) the parent isotope distribution (and whether they are expected to influence one or more daughter nuclide distributions), (2) the degree of partitioning of Pb between clustered domains and surrounding zircon, (3) the initial Pb isotope composition (concentration and initial ratio) of the specimen and the "bulk" Pb evolution since crystallization, and (4) the relationship between the rate of Pb migration and duration of the migration event. Despite several simplifications in the age model derived above (eqns. 1-6), the need to incorporate increasingly complex elements into this age model is based, in part, on the achievable analytical accuracy and precision for  $^{207}$ Pb/ $^{206}$ Pb ratios from APT data, and the spatial heterogeneity present in the data sets.

## 2 Samples and Methods

Zircon BT5-13 is a 3.77 Ga detrital zircon from the Beartooth Mountains, Montana, originating from an Archean quartzite lens within the Quad Creek/Hellroaring Plateau region (Fig. 1). *Mueller* et al. [1992] documented concordant zircon domains up to 4.0 Ga within these quartzite lenses, and proposed a depositional age for the quartzite host of ~3.3 Ga. These rocks have persisted through several periods of deformation and metamorphism, including granulite facies metamorphism at ~3.25-3.1 Ga, subsequent retrograde amphibolite facies metamorphism [e.g., *Henry* et al., 1984], and local intrusion of the Long Lake igneous complex [*Mueller* et al., 1988]. Zircon BT5-13 was selected for APT study based on (1) homogeneous U and Th concentrations, and (2) two, 100% concordant SIMS U-Pb age analyses within the core with  $^{207}$ Pb/ $^{206}$ Pb ages of 3778 ± 16 Ma and 3772 ± 10 Ma (±2 $\sigma$ ).

EBSD point mapping of BT5-13 shows crystallographic/structural trends generally consistent with the compositional trends observable in backscattered electron (BSE) and cathodoluminescence (CL) imaging (see Fig. 1 for EBSD summary, and Table 1 for EBSD analysis information). The zircon core possesses oscillatory and sector zoning typical of igneous zircon, surrounded by discontinuous concentric fractures separating the zircon core from an oscillatory zoned, bright in BSE (dark in CL) rim domain. Within the rim, fine scale fractures are visible, along with intermittent patches where BSE and CL contrast locally crosscuts oscillatory bands. Some of these rim features contain numerous micron-scale inclusions; combined with the patchy BSE and CL contrast, and the poor band contrast in EBSD, this is taken as evidence that

the rim domain is partially to fully metamict and preserves a complex history of damage accumulation plus/minus recrystallization. (We note that band contrast is a measure of the contrast difference between the bands and background within the electron backscatter diffraction pattern; as such, it is a complex function of sample characteristics including sample polish/preparation, crystal structure, crystallinity, etc. and thus no quantitative measure of the present structural state ("effective" alpha dose) for BT5-13 is attempted based on this information.) Within the core, small ( $<2^{\circ}$ ) relative misorientations are associated with fractures, though the exact timing of fracturing is unknown. Important to this study is the lack of any discernable misorientation or crystallographic complexity within the domain sampled by atom probe lift-out (Fig 1a). Closed system U-Pb systematics, dominantly igneous textures in SEM imaging, and uniform crystallography by EBSD, are taken as strong evidence for closed system chemical behavior on the micron scale throughout the zircon core region. This is in spite of the fact that the calculated dose from radioactive decay of U and Th is  $7.1 \times 10^{15}$   $\alpha$ -decays/mg over the 3.77 Ga history of the zircon, well above that required to exceed the first percolation point in the absence of annealing ( $\sim 1-2 \times 10^{15} \alpha$ -decays/mg [e.g., Ewing et al., 2003]). We do not know, in detail, the structural state of zircon BT5-13 as a function of time (i.e., annealing rate as a function of time, preservation of distinct damage structures, etc.); however, the U-Pb systematics from SIMS suggest that high temperature events within BT5-13's history (including, but perhaps not limited to, granulite facies metamorphism) did not coincide with a significantly damaged crystal structure in the zircon core. If this were the case, we would expect micron scale Pb mobility, and more complex U-Pb systematics.

Three needle-shaped specimens were prepared from a single FIB (focused ion beam) liftout taken from the core of the zircon, with the long axis of the specimens normal to the imaged surface in Fig. 1a; the lift-out was deliberately taken along visible banding to limit compositional and structural variability between adjacent atom probe specimens. Needle-shaped specimens were run on a LEAP 5000 XR (local electrode atom probe, with reflectron) at the CAMECA Atom Probe Technology Center in Madison, Wisconsin in laser pulsing mode. Run conditions and data reconstruction are summarized in Table 2. Two of the three specimens survived through the end of analysis. Reconstructions, ranging and cluster analysis have been performed using CAMECA's Integrated Visualization and Analysis Software (IVAS 3.6.10), with mass spectra showing consistent behavior from specimen-to-specimen (Fig. 2). The reconstruction of data sets was approached individually and iteratively, utilizing spectral ranges refined during preliminary reconstruction and data analysis. Reconstruction optimization held constant those parameters measured as part of pre- and post-acquisition imaging (sphere-cone radius ratio, shank angle, final end-tip radius, etc.) and aimed to reproduce the inferred dimensions of evaporated material, as estimated from pre-/post-analysis imaging. The bulk composition is consistent with that of zircon, with Hf, Y, Yb, and Pb constituting the detectable minor and trace elements. Pb isotopes appear as doubly charged ions within the mass spectrum (Fig. 2); no singly charged ions are detectable at 204, 206, 207 and 208 Da. There is no detectible <sup>204</sup>Pb<sup>2+</sup> at 102 Da, and <sup>208</sup>Pb<sup>2+</sup> occurs along with an isobaric interference from <sup>28</sup>Si<sub>2</sub><sup>16</sup>O<sub>3</sub><sup>+</sup> at 104 Da. No attempt at decomposing this interference is made here.

Each of the three APT data sets contain several sub-15 nm domains, enriched by a factor of  $\sim 10^2$ - $10^3$  over the surrounding matrix (Fig. 3). While these domains are similar in size and shape to other clusters in zircon [e.g., *Valley* et al., 2015; *Peterman* et al., 2016], they are distinct in that only some clusters possess a colocalization of Y, P and other REE. Although Pb-rich

domains are not numerous, Pb is sufficiently concentrated in clusters that that they may be reliably isolated based directly on the spatial distribution of Pb.

## 2.1 Cluster Analysis

For any given APT data set, the absolute number of clusters, their dimensions and the total number of constituent atoms in each is, strictly speaking, dependent upon the cluster identification protocol and protocol inputs [e.g., Gault et al., 2012]. In order to evaluate the dependence of observed isotope ratios on the cluster definition (i.e., whether there is statistically significant spatial variability in Pb-isotope ratios), Pb-rich domains are isolated using six permutations of the two most common cluster identification methods: kth order Nearest Neighbor cluster analysis (kNN), and isoconcentration surfaces [e.g., Gault et al., 2012; Larson et al., 2013]. Cluster analysis is completed using IVAS 3.6.10 (see Table 2). Each cluster analysis permutation is applied to individual data sets, and the Pb-rich regions in the different data sets are concatenated to produce a composite mass spectra for the complete set of equivalently-defined BT5-13 clusters. In defining isoconcentration surfaces, several different delocalization and voxelation permutations were explored. Because Pb is a dilute component (particularly in the matrix) isoconcentration surface position and morphology becomes particularly sensitive to small fluctuations in Pb ion positioning when voxel sizes are too small, and when the delocalization is highly localized [e.g. Larson et al., 2013]. For all datasets, a voxel size of [1.0, 1.0, 1.0] nm and a delocalization of [6.0, 6.0, 3.0] nm in the [x, y, z] dimensions describes the general cluster extent and shape, and effectively smooth the high-density layering associated with complex field evaporation behavior (see Fig. 3, and discussion below). For  $\kappa NN$ cluster analysis, algorithm inputs were calibrated for each individual data set following the general methodology guided by  $\kappa NN$  distributions (Fig. 4), cluster size distributions, and cluster count distributions [e.g., Larson et al., 2013]. The nearest neighbor distances between Pb atoms are determined for order parameters,  $\kappa$ , between one and ten (Fig. 4). At each  $\kappa$ , two peaks are observed; one at smaller Pb-Pb distances associated with Pb in clusters, and a peak at larger distances associated with Pb-Pb distances between more dilute Pb in the matrix. A third peak can be seen at very small Pb-Pb distances in two data sets, which occurs when a large proportion of clustered Pb atoms are reconstructed within high density layers. Given the broad separation of peaks associated with clustered and matrix Pb for  $\kappa$ >2,  $\kappa$ NN cluster analyses were completed for orders  $\kappa=2, 3, 4, 5$  (Fig. 4). For each  $\kappa$ NN analysis, the maximum separation parameter,  $d_{\text{max}}$ , was taken to be the approximate minimum between the matrix and clustered Pb peaks in the nearest neighbor distribution. Following the rationale of *Chen* et al., [2014] we take the envelope parameter,  $L=d_{\text{max}}$ , and the erosion parameter, E, equal to  $d_{\text{max}}$  minus the maximum for the clustered Pb distribution. The consistent calibration of algorithm inputs, rather than unilateral application of a single set of inputs, helps to minimize any systematic differences between data sets introduced during data reconstruction. We note that the details of the reconstruction introduce uncertainties in the absolute position of ions and can generate systematic error in the absolute size and shape of clusters. As a result,  $\kappa NN$  algorithm inputs, and the position of a given isoconcentration surface, may vary slightly based on the exact reconstruction. This said, small changes in the reconstruction will result in small changes to the *relative* position of closely spaced (nearest neighbor) ions. This, combined with a consistent calibration of the  $\kappa NN$ 

algorithm inputs for each individual data set is expected to mitigate the dependence of observed isotope ratios to small variations in reconstruction parameters.

## 2.2 Ranging and Uncertainties

Determination of Pb isotope ratios and uncertainties requires the calculation of Pb isotope signals and the propagation of uncertainties, both those resulting from counting statistics and those resulting from data reduction. The  $^{206}$ Pb<sup>2+</sup> and  $^{207}$ Pb<sup>2+</sup> signals ( $^{206}$ S and  $^{207}$ S, respectively) are calculated from the background correction of the total integrated peak counts ( $^{206}$ T and  $^{207}$ T) in the 103 and 103.5 Da peaks, respectively:

$$S = T - B \tag{7}$$

Accurate isotope ratios (<sup>207</sup>Pb/<sup>206</sup>Pb = <sup>207</sup>S/<sup>206</sup>S = <sup>207</sup>Pb<sup>2+</sup>/<sup>206</sup>Pb<sup>2+</sup>) requires that the same fraction of each signal is integrated, and this is influenced by (1) the placement of integration bounds, and (2) characterization and correction of counts for peak overlaps/interferences. In order to evaluate the reproducibility of measured signal levels and their sensitivity to various parameters, this work utilizes a series of ranging protocols to identify peak integration bounds for the 103.0 and 103.5 Da peaks. In general, Pb isotope signals levels and signal-to-noise ratios vary significantly based on the data set and analytical volume. We explore two different ranging schemes that incorporate different assumptions of spectral complexity. In situations of well-separated peaks where peak overlaps are either absent or obscured, a simple ranging scheme can often be applied that identifies range bounds relative to the local background. In cases where peak tails are present or peak overlaps do not allow for a simple statistical approach, modeling of peak shapes can allow for both placement of range bounds and correction of counts within neighboring peaks for a more accurate estimation of signals.

In cases where peak overlaps are ignored, we identify peak integration bounds by identifying the continuous domain (for each peak) for which all individual bins exceed some statistical threshold; this threshold is function of the local background, and the desired confidence level. In this work, the average background level per bin,  $B_1$ , and the standard deviation,  $\sigma_{B,1}$ , are calculated from the featureless portion of the spectrum between ~102.25 Da and ~102.75 Da. Because the background is well-described by Poisson statistics [Larson et al., 2013],  $\sigma_{B,1} \approx \sqrt{B_1}$ . While several different statistical thresholds can be used in to define ranges, we explore use of the critical level,  $L_C$ , and detection level,  $L_D$ , as discussed by [Currie, 1968]. The critical level can be considered the level at which counts exceed the background at some confidence level, and the detection level can the considered the level at which a signal is "detected" (i.e. exceeds the critical level) with a specified confidence level.

In establishing whether a single bin is included within the integrated signal, we start at the nominal peak position (103.0 and 103.5 Da, respectively) and move to the high or low side, considering counts in the *i*th bin relative to the threshold value,  $C_1$  (Fig. 5). Determining  $L_C$  and

 $L_D$  require consideration of the uncertainty in  $S_i$  (the signal in a single bin) as  $S_1 \rightarrow 0$ , which is given by:

$${}^{207}S_{1} = {}^{207}T_{1} - B_{1} \quad (8a)$$

$${}^{207}\sigma_{S0} = \sqrt{{}^{207}T_{1} + B_{1}} = \sqrt{({}^{207}S_{1} + B_{1}) + B_{1}} = \sqrt{2B_{1}} = \sqrt{2} \sigma_{B,1} \quad (8b)$$

$${}^{206}S_{1} = {}^{206}T_{1} - B_{1} \quad (9a)$$

$${}^{206}\sigma_{S0} = \sqrt{{}^{206}T_{1} + B_{1}} = \sqrt{({}^{206}S_{1} + B_{1}) + B_{1}} = \sqrt{2B_{1}} = \sqrt{2} \sigma_{B,1} \quad (9b)$$

When  $C_1$  is set equal to  $L_C$  (i.e., bins where  $C_i > C_1 = L_C$  are statistically above the background level for a given confidence level),  $C_1$  becomes [Currie et al., 1968; Larson et al., 2013]:

$$^{207}C_1 = L_C = B_1 + k^{207}\sigma_{S0} = B_1 + k\sqrt{2}\sigma_{B.1}$$
 (10)

$$^{206}C_1 = L_C = B_1 + k^{206}\sigma_{S0} = B_1 + k\sqrt{2}\sigma_{B1}$$
 (11)

Where k represents the quantile for a given (single tailed) confidence level. We use a confidence level of 95%, corresponding to k=1.645; this represents the level at which there is only a 5% chance of  $C_i$  exceeding  $B_1 + k\sigma_{S0}$  when no signal is present. On the low-m/n side of each peak, the range bound is identified as the outermost bin (relative to peak center) for which counts in the ith bin,  $C_i$ , exceed  $C_1$ , while  $C_{(i-1)}$  does not (Fig. 5b). On the high side, range bounds are set at the outermost bin (relative to the peak center) for which  $C_i > C_1$  exceed the cutoff, while  $C_{(i+1)}$  does not. When  $C_1$  is set equal to  $L_D$ , (i.e. the point at which signal in the signal in t

$$^{207}C_1 = L_D = B_1 + k^2 + 2k^{207}\sigma_{S0} = B_1 + k^2 + 2k\sqrt{2}\sigma_{B.1}$$
 (12)

$$^{207}C_1 = L_D = B_1 + k^2 + 2k^{207}\sigma_{S0} = B_1 + k^2 + 2k\sqrt{2}\sigma_{B,1}$$
 (13)

where we again set k=1.649, corresponding to a single tailed confidence level of 95%. Analogous to above, this represents where there is only a 5% chance of  $C_i$  exceeding  $L_D$  when the true signal is less than  $(L_C - B_1)$ .

In the approach above, we have assumed that the 103.0 and 103.5 Da peaks share a common background level and there is no statistically significant tail on the 103.0 Da peak which contributes to the 103.5 Da peak (discussed in more detail below). In this simple case, the

background counts integrated in each peak ( $^{206}B$  and  $^{207}B$ ) and their uncertainties ( $^{206}\sigma_B$  and  $^{207}\sigma_B$ ) can be calculated from  $B_1$  and  $\sigma_{B,1}$ :

$${}^{207}B = B_1 n_{bin,207} \qquad (14a)$$

$${}^{207}\sigma_B = \sqrt{{}^{207}B} = \sqrt{B_1 n_{bin,207}} = \sigma_{B,1} \sqrt{n_{bin,207}} \qquad (14b)$$

$${}^{206}B = B_1 n_{bin,206} \qquad (15a)$$

$${}^{206}\sigma_B = \sqrt{{}^{206}B} = \sqrt{B_1 n_{bin,206}} = \sigma_{B,1} \sqrt{n_{bin,206}} \qquad (15b)$$

For any given spectrum, this procedure is a simple way to statistically identify range bounds, assuming well-separated peaks with minimal signal in peak tails. We repeat this procedure at spectral binnings between 0.001 to 0.045 Da, in increments of 0.001 Da, in order to ascertain the variability in measured signal and calculated ratios associated with spectral binning. This range of bin widths form a continuum between overly fine bin widths (highly resolved bins with significant noise), through well-defined peak shapes, to overly coarse bin widths having oversimplified peak shapes. Each of these spectra are representations of the same underling data, but with different effective smoothing and count levels (per bin). The calculation of isotope ratios can be done at any spectral binning, though for reasons discussed below, there are practical considerations in the range of bin widths that will generate accurate and precise ratios, and how sensitive a ranging approach is to bin width.

This general procedure is a pragmatic approach that balances several aspects of the ranging process, and can be consistently and reproducibly applied to both the 103.0 and 103.5 Da peaks. This said, Pb isotope signals remain a function of integration bounds, and there exists some uncertainty in the placement of bounds within real data, particularly in cases where integrated signal level approach the limits of detection, and thus a large number of bins within a given peak occur at or near  $L_C$  (or  $L_D$ ). If peak overlaps are considered negligible, accurate determination of isotope ratios requires that equivalent proportions of each peak be integrated. For a single peak, wider integration bounds will integrate more of the peak and will (1) include a better estimate of the true signal (while incorporating additional uncertainty from background correction) and (2) be less sensitive to spectral characteristics (bin width, etc.). Uncertainty in ranging of peaks can be estimated by integrating a proportionally wider region of the two peaks, and comparing this ratio to that calculated initially. If, for example, the 103.5 peak was significantly "under-ranged," then there will be a larger shift in  $^{207}S$ , and increase in the  $^{207}Pb/^{206}Pb$  ratio. If the range bounds defined based on  $L_C$  (or  $L_D$ ) integrate regions  $^{206}\eta_1$  and

 $^{207}\eta_1$ , we integrate an additional 25% of each peak on both the high and low side, and estimate  $\sigma_{ranging}$  (Fig. 5d):

$$\sigma_{7/6,\text{ranging}} = \frac{\binom{207}{\text{Pb}}/206}{\binom{207}{\text{Pb}}/206} \frac{1}{\text{Pb}} - 1 \quad (16)$$

This uncertainty can be propagated along with uncertainties from counting statistics and background correction to represent a more complete uncertainty in the measured <sup>207</sup>Pb/<sup>206</sup>Pb ratio.

We note that for the BT5-13, there exists a subset of the spectral binnings for which the identified range bounds result in the total number of bins *between* the  $^{206}\eta_1$  and  $^{207}\eta_1$  ranges is less than ( $^{206}\eta_1 + ^{207}\eta_1$ )/4 (Fig. 5). While this is a natural product of how counts are distributed within bins, there would be overlap in the regions integrated by  $^{206}\eta_2$  and  $^{207}\eta_2$ , and thus the counts within such a region would result in "double counting" of some spectral bins. In such situations, the counts between  $^{206}\eta_1$  and  $^{207}\eta_1$  are divided equally between  $^{206}\text{Pb}$  and  $^{207}\text{Pb}$  in order to avoid this complexity. From an analytical standpoint, more of the counts between the two peaks have been attributed (according to the ranging procedure above) as either  $^{207}\text{Pb}^{2+}$  or  $^{206}\text{Pb}^{2+}$  in placement of  $^{206}\eta_1$  and  $^{207}\eta_1$ , and the effective uncertainty in integrated signal as a function of the middle two integration bounds decreases.

In calculating the total uncertainty in the  $^{207}\text{Pb}/^{206}\text{Pb}$  ratio,  $\sigma_{7/6}$ , we propagate errors originating from counting statistics, background correction and ranging:

$$^{207}\sigma_{S} = \sqrt{^{207}\sigma_{CS}^{2} + ^{207}\sigma_{B}^{2}} = \sqrt{^{207}T + B_{1}n_{bin,207}}$$
(17)

$$^{206}\sigma_{S} = \sqrt{^{206}\sigma_{CS}^{2} + ^{206}\sigma_{B}^{2}} = \sqrt{^{206}T + B_{1}n_{bin,206}}$$
 (18)

$$\sigma_{7/6} = \sqrt{\frac{207}{\sigma_S}^2 \left(\frac{\partial R_{76}}{\partial z^{07}S}\right)^2 + \frac{206}{\sigma_S}^2 \left(\frac{\partial R_{76}}{\partial z^{06}S}\right)^2 + \sigma_{7/6,ranging}^2}$$
(19)

Where  $^{207}\sigma s$  and  $^{206}\sigma s$  are uncertainties in  $^{207}S$  and  $^{206}S$  from background correction and counting statistics, and  $\sigma_{7/6, ranging}$  is the uncertainty from eqn. (16) above.

For the BT5-13 cluster data sets, there do exist small, but observable, tails on the highm/n side of the 103.0 and 103.5 Da peaks. The signal levels within these tails are sufficiently small to permit the ranging and background correction scheme above to largely ignore this complexity; however, qualitatively speaking there is a loss of accuracy when this is unaccounted for, both in determining the most accurate <sup>206</sup>S and <sup>207</sup>S, but also in correcting <sup>207</sup>S for <sup>206</sup>Pb<sup>2+</sup> ions within the 103.0 Da peak tail. We look to treat this aspect of ranging for two reasons: (1) to evaluate the difference in <sup>207</sup>Pb/<sup>206</sup>Pb ratio when accounting for and correcting counts based on peak tails, and (2) the general occurrence of higher backgrounds, larger peak tails and peak

overlaps can necessitate accounting for these spectral features in order to derive accurate and precise <sup>207</sup>Pb/<sup>206</sup>Pb ratios. We explore alternative means to define the range bounds and correct signal levels associated with the 103.0 and 103.5 Da peak for situations where peak tails are more pronounced.

Here, the modeling of peak tails to calculate signal levels and correct peak overlaps is approached very generally; there exists no analytical peak form for fitting of peaks (or peak tails) given peak shapes vary as a function of numerous variables including specimen properties (e.g., material properties, specimen geometry, etc.), instrument configuration (e.g., straight flight path vs. reflection geometry), run conditions (specimen base temperature, laser spot size, laser pulse energy, pulse frequency, etc.) and spectral calibration [e.g., Kellogg and Tsong, 1980; Bunton et al., 2007]. The time dependence of field evaporation varies between samples, given that each specimen possesses small differences in geometry, which in turn influences the thermal response of the specimen during laser pulsing. Strictly speaking, these differences in thermal behavior will manifest as small differences in peak shapes between various mass spectra. While several studies have fit peak tails based on numerical modeling of peak thermal evolution which incorporates geometric and material properties of the specimens [e.g., Vurpillot et al., 2004; Bunton et al., 2007; Bachkav et al., 2011] these methods are not as suitable for evaluation of concatenated spectra, sourced from multiple specimen (such as those analyzed here). In light of this, we fit background corrected peak tails on the high-m/n side of the 103.0 and 103.5 Da peaks, starting at approximately the full width at tenth maximum, using a functional form:

$$C = a_1 \exp(a_2 x^p) \tag{20}$$

Where  $a_1$ ,  $a_2$ , and p are fit constants, and x is the mass-to-charge state ratio. The general purpose of our modeling is estimation, correction and calculation of Pb isotope signals, and we stress that the general procedure presented here is not dependent upon this peak shape model, and can be implemented and/or adapted using a variety of fitting functions or with more robust modeling of peak forms (e.g., thermal modeling of peak tails).

Calculating signal levels and isotope ratios using fits to the peak tails follow a similar approach to the procedure presented above, but with several adaptations (Fig. 6). Peak fitting and placement of range bounds is approached using an iterative background stripping scheme; the background corrected fit to the 103.0 Da peak tail is used to correct the 103.5 Da peak for  $^{206}$ Pb, and the tail of the 103.5 Da peak is then fit. The fits to the corrected spectra are used to establish integration bounds within the peak tails by establishing when the fit drops below the critical limit,  $L_C$ . The low-side integration bounds of each peak are placed analogous to above: by finding for the continuous range where  $C_i > C_I = L_C$ ; however, because we now treat the 103.5 Da peak as sitting on the tail of the 103.0 Da peak, the "background" relevant for establishing

significant  $^{207}\text{Pb}^{2+}$  counts requires consideration of 103.0 Da peak tail (in this case, the fit of the 103.0 peak tail). Thus,  $^{207}C_{1,i}=L_C$  is a function of position within the peak tail, and becomes:

$${}^{207}C_{1,i} = (B_1 + {}^{206}S_{i,fit}) + k^{207}\sigma_{S0} = (B_1 + {}^{206}S_{i,fit}) + k\sqrt{2}\sqrt{(\sigma_{B,1}{}^2 + {}^{206}S_{i,fit})}$$
(21)

where  ${}^{206}S_{i,fit}$  is the modeled  ${}^{206}Pb^{2+}$  signal in the *i*th bin.

The <sup>207</sup>Pb<sup>2+</sup> and <sup>206</sup>Pb<sup>2+</sup> signals are calculated by summing the spectra between the designated integration bounds, and correcting for both background counts and modeled peak overlaps. This procedure is repeated at bin widths of data between 0.001 Da and 0.045 Da, in increments of 0.001 Da. Fitting of peak tails is used principally for placement of range bounds, and correction of the 103.5 Da peak (Fig. 6); <sup>206</sup>Pb<sup>2+</sup> signal levels are estimated from the peak fit *only* in the small number of cases where the fitting of the peak tail results in peak integration bounds which overlap. We do not attempt to estimate the uncertainty in signal levels associated with placement of range bounds for the 103.0 or 103.5 Da peaks based on fitting. Because counts within the <sup>207</sup>Pb and <sup>206</sup>Pb tails are small, these errors will be minimal and do not influence the conclusions below; however, this may be an important source of uncertainty in cases where larger peak overlaps occur.

Accounting for the estimated <sup>206</sup>Pb<sup>2+</sup> contribution to the 103.5 Da peak, the total uncertainty in the <sup>207</sup>Pb/<sup>206</sup>Pb ratio then becomes:

$$^{207}\sigma_{S} = \sqrt{^{207}\sigma_{CS}^{2} + ^{207}\sigma_{B}^{2}} = \sqrt{^{207}T + \left(B_{1}n_{bin,207} + \sum_{i}^{n} ^{206}S_{i,fit}\right)}$$
(22)
$$^{206}\sigma_{S} = \sqrt{^{206}\sigma_{CS}^{2} + ^{206}\sigma_{B}^{2}} = \sqrt{^{206}T + B_{1}n_{bin,206}}$$
(23)
$$\sigma_{7/6} = \sqrt{^{207}\sigma_{S}^{2} \left(\frac{\partial R_{76}}{\partial ^{207}S}\right)^{2} + ^{206}\sigma_{S}^{2} \left(\frac{\partial R_{76}}{\partial ^{206}S}\right)^{2}}$$
(24)

One spectral complication that is not treated here is the potential of a <sup>206</sup>Pb<sup>1</sup>H<sup>2+</sup> contribution to the 103.5 Da peak. This interference cannot be resolved within this data and the magnitude and nature of hydride interferences remains an active area of research. We follow the rationale of *Valley* et al., [2015] that doubly charged hydride ions are rare and consider this contribution negligible for the analytical precision determined here.

#### 3 Results and Discussion

#### 3.1 Cluster Analysis

The consistent application of clustering algorithms isolates broadly similar regions within the three BT5-13 data sets, though different approaches generate small differences in the total number of clusters, their size, and the total number of Pb atoms (Fig. 7-9, Table 3). The similarity between the different approaches is somewhat expected given the  $10^2$  to  $10^3$  relative

enrichment of Pb within most clusters, and the relatively sharp boundary between clusters and matrix. Several smaller, more dilute clusters are identified within the M5\_491 and M1\_568 data sets; these small clusters are largely excluded when using the higher concentration 0.5% atom Pb threshold for the isoconcentration surfaces. As will be discussed later, both the small total number of clusters, and the small total number of Pb atoms within smaller more dilute clusters, make it difficult to identify a definitive difference in phase relations, genesis, or timing of formation relative to larger clusters. The consistent application of the  $\kappa$ NN cluster algorithm led to identification of all clusters >0.25 atom% Pb, though parsing data for individual clusters still allows one to discern a general difference in low- vs. high-Pb clusters.

Several of the large clusters possess a high density of reconstructed ions (all ions, not only Pb) in layers on the upper surface of the Pb-rich domains (Fig. 3); similar features have been observed before [e.g., Peterman et al., 2016] and are associated with increased evaporation of constituent atoms upon exposure of the Pb-rich domains at the surface of the specimen. It is evident that Pb-rich domains possess a distinct evaporation field relative to the surrounding zircon. Whether these domains constitute a distinct nanoscale phase within the BT5-13 zircon remains unclear based on the present data. The Pb-rich domains have an approximate "zircon composition" based on the Zr, Si, and O, however they contain up to 3% atomic Pb. The comparison of bulk APT compositions and those of clusters, suggest that Pb is accommodated by a decrease in Zr, as reported by Valley et al., [2015]. As noted above, the quantitative compositional analysis, particularly of complex oxides, remains an active area of research, and while the evaporation behavior and composition are distinct from those of the surrounding zircon, the structure, accommodation, and detailed composition of these nanoscale domains requires further study. These details have important implications for the genesis and origin of clusters; however, given high density layers are associated with clusters and are identified as such by the approaches above, these details are largely independent of the *analytical* limitations on Pb isotopic measurement discussed here.

# 3.2 Ranging and <sup>207</sup>Pb/<sup>206</sup>Pb ratios

Within the concatenated BT5-13 cluster data sets, signal-to-background ratios are relatively high (between 20-85), and  $^{207}\text{Pb}^{2+}$  and  $^{206}\text{Pb}^{2+}$  signal levels are within 30% of one another. For any given cluster definition, all three ranging approaches generate relatively consistent trends for signal levels and isotope ratios as a function of bin width (representative data for the 0.5% atomic Pb clusters is shown in Fig. 10). At very fine bin widths, ranged signals are systematically low, particularly for range definitions based on  $L_C$  and  $L_D$ . As bin width increases, signal levels increase and stabilize at an approximately constant level, with the signal level, and scatter in the signal level, being dependent on the ranging approach. Ranging based on fitting of peak tails is less sensitive to bin width, as it effectively smooths data as the signal within the peak tails approaches the background. The measured  $^{207}\text{Pb}/^{206}\text{Pb}$  ratios possess similar trends to those of the signal levels: ratios are low and scattered at fine bin widths where there is increased scatter in ranged  $^{206}\text{Pb}^{2+}$  and  $^{207}\text{Pb}^{2+}$  signal levels, and the ratios stabilize as binning becomes coarser. Importantly, only data at fine bin widths are statistically distinct from the majority of isotope ratios.

Each ranging approach above possesses advantages and disadvantages which are not independent of the signal levels and background levels inherent in the data. Basing ranges on  $L_D$ 

is simpler to apply to data sets, however, this approach generates thinner ranges and includes fewer counts from peak edges where counts approach the background level. The thinner ranges result in isotope ratios which possess more scatter as a function of bin width; the  $2\sigma$  scatter in isotope ratios as a function of bin width between 0.010 and 0.045 Da bin widths (filled circles in Fig. 10) is 0.008 or just under 2%. This can be compared to ranges based on  $L_C$  and fitting of peak tails which each possess  $2\sigma$  scatter of 0.008 (1.1%) over the same range in bin widths. These differences make intuitive sense, as thinner ranges are more sensitive to the distribution of counts within bins at any given bin width. While all three ranging approaches are likely to generate accurate isotope ratios, ranges based on  $L_C$  and fitting of peak tails are considered more reproducible and precise. Because peak overlaps are largely negligible, these two approaches produce virtually identical measured  $^{207}\text{Pb}/^{206}\text{Pb}$  ratios for the signal levels and isotope ratios within the BT5-13 cluster data sets. Both of these procedures are capable of identifying consistent signal and isotope ratios in cases where peak overlaps are minimal, and while the work here demonstrates how fitting and ranging may work in practice for overlapping peaks, the accuracy of this decomposition (as it pertains to  $^{207}\text{Pb}/^{206}\text{Pb}$  ratios) requires further testing.

The results above demonstrate that for bin widths that are not overly fine, the ranging approaches above generate consistent ratios which are statistically equivalent over a broad range of bin widths. For each cluster definition, representative ratios at or near the mean of ratios between 0.010 Da and 0.045 Da bin widths is summarized in Table 3. All of the ranging approaches (Lc,  $L_D$ , Fit) for all the cluster definitions (2CA, 3CA, 4CA, 5CA, 0.25 % atomic Pb, 0.5% atomic Pb) result in statistically identical  $^{207}$ Pb/ $^{206}$ Pb isotope ratios, varying between 0.794±0.15 (±2 $\sigma$ ; 470 atoms) and 0.715±0.052 (3343 atoms). While the consistency of ratios give the appearance of a "systematic offset" between the  $\kappa$ NN cluster analysis and isoconcentration surface cluster definitions, this difference cannot be considered statistically significant. The most direct comparison of the Pb isotope structure of clusters, is between the 0.5 atom% Pb isosurface and 0.25 atom% Pb isosurface definitions, with these results indicating identical Pb isotope ratios within uncertainty.

For the BT5-13 clustered data sets, counting statistics are the largest contributor to uncertainty in the <sup>207</sup>Pb/<sup>206</sup>Pb ratios. Maximizing detection efficiency based on technological advances and/or instrument geometry may serve as a means to collect a larger number of ions for the same volume, and improve the precision of Pb isotope ratios. For the LEAP 5000 series of instruments manufactured by CAMECA Inc., nominal detection efficiencies are 50% and 80% for the reflection and straight flight path geometries, respectively. The data presented here were collected on a LEAP 5000 XR (reflection geometry) and an increase in Pb counts by 60% has potential to improve aspects of precision in APT Pb isotope determinations. However, the consistency in isotope ratio determination here benefits from well-defined and well-separated peaks; the increase in detection efficiency is balanced by broader peaks and other aspects of spectral analysis, such as fitting and constraining peak overlaps, may become increasingly important (and perhaps limiting) aspects of <sup>207</sup>Pb/<sup>206</sup>Pb analysis by APT.

Signal-to-noise ratios within the bulk data sets are far lower than those of the clusters, with  $^{207}\text{Pb}$  approaching the statistical detection limit; these factors drastically alter the applicability of the ranging approaches outlined above. For the concatenated bulk data sets (i.e., bulk data for all three specimens), ranging based on  $L_C$  results in  $^{207}\text{Pb}/^{206}\text{Pb} = 0.191 \pm 0.080$  (2 $\sigma$ ). This value is statistically distinct from that measured by SIMS (for spot BT5-13-2:

 $^{207}$ Pb/ $^{206}$ Pb = 0.3675 ± 0.0037; ( $^{207}$ Pb/ $^{206}$ Pb)\* = 0.3666 ± 0.0044, 2 $\sigma$ ) and we do not assign significance to this ratio derived from APT for several reasons: (1) low signal-to-noise results in  $^{207}$ Pb/ $^{206}$ Pb ratios which are much more sensitive to bin width and ranging, (2) the lower relative signal-to-noise for the 103.5 Da peak leads to a systematic "under-ranging" when applied based on Lc (thus the calculated ratio is considered inaccurate), and (3) the uncertainty in background correction (particularly for  $^{207}$ Pb) becomes the largest contributor to overall uncertainty. The relevance of this last point is particularly clear when considering that, while they are within uncertainty,  $^{207}$ Pb counts within clusters exceed the total  $^{207}$ Pb counts determined within the bulk data set (Table 3). Poorly resolved peak shapes (due to much higher background) makes peak fitting untenable, and fitting was not attempted on the bulk data sets.

Due to the above factors, we have also ranged the 103.0 and 103.5 Da peaks "by hand", holding constant the integration bounds and correcting each peak using the background level *directly adjacent* (as opposed to using a single background range between ~102.25 and ~102.75 Da). This results in an isotope ratio of  $^{207}$ Pb/ $^{206}$ Pb=0.353 ± 0.18 (2 $\sigma$ ), excluding any estimation of errors due to ranging (Table 3; Fig. 11). These data are relatively imprecise, and as such it is difficult to ascribe them geological significance; however, these data are both (1) a striking match to SIMS based  $^{207}$ Pb/ $^{206}$ Pb measurements, and (2) significantly lower than isotope ratios within clusters. This may be (cautiously) treated as supporting evidence in favor of closed system U-Pb systematics on the micron scale (within the zircon core). For BT5-13, the strongest evidence for this is the uniform chemical and isotopic composition within the zircon core measured by SIMS.

The data sets above highlight both the strengths and limitations of statistical or fit based ranging (as they are applied here). Most notably the statistical and fit based approaches become increasingly unreliable for isotope ratio determinations as signals approach the limits of detection, particularly if this occurs for one isotope but not another. It remains true that there is no singular method for ranging, and the relevant uncertainties and limits of interpretation must be considered on a data set-by-data set (and spectrum-by-spectrum) basis. The approaches outlined above in section 2.2 are well-suited for reproducible measurement of Pb isotope ratios, and the appropriate uncertainties, for data at moderate to high signal-to-noise levels. In general, peak fitting is considered the most likely to result in accurate and precise signals, as this approach effectively smooths data as it approaches the background, and allows for estimation of overlapping signals in adjacent 103.0 and 103.5 Da peaks; however, in such a situation, range bounds become dependent upon data fitting, and thus the functional form/method used in fitting peak tails. An in-depth investigation of this type of analysis is beyond the scope of this paper. In general, the analysis above supports the general considerations for ranging presented elsewhere [e.g., Larson et al., 2013]. For "well-separated peaks" (taken here to mean those peaks where  $C_i$ drops below  $L_c$  between peaks) with moderate signal-to-noise ratios, reasonable ranges that include a large percentage of the <sup>207</sup>Pb<sup>2+</sup> and <sup>206</sup>Pb<sup>2+</sup> signals should generate reproducible <sup>207</sup>Pb/<sup>206</sup>Pb ratios within error; errors due to background correction and counting statistics should provide a good estimate of the total uncertainty in <sup>207</sup>Pb/<sup>206</sup>Pb. In cases where peak overlaps are

present, peaks are not well-separated, or geological interpretations are at the limits of these uncertainties, consideration of other factors limiting accuracy and precision may be required.

# 3.3 Model Ages for Cluster Formation:

Above, we have been largely concerned solely with spatial and spectral aspects of measuring <sup>207</sup>Pb/<sup>206</sup>Pb isotope ratios; here we look to make first order interpretations about their geological significance. Given the systematic trends in bulk and clustered Pb ratios in the BT5-13 data sets, clustered Pb is taken to represent ancient reorganization of radiogenic Pb; as discussed above, the timing of Pb mobility and cluster formation can be modeled based on cluster <sup>207</sup>Pb/<sup>206</sup>Pb ratios. We make several simplifications in calculating "model cluster ages." Firstly, we assume the initial Pb component is vanishingly small and thus all Pb within the APT data is radiogenic in origin; this is supported by no detectable <sup>204</sup>Pb at 102 Da within the APT data, and the low level of common Pb within SIMS analyses. We also assume there was complete partitioning of Pb into cluster domains at  $t_2$  (within analytical uncertainty), and  $X'_{Pb,t2}$  $\rightarrow$ 1 (i.e.,  $^{207}$ Pb/ $^{206}$ Pb ratios within clustered domains represent the isotope ratios of cluster Pb at t2: eqn. (5,6)). The partitioning behavior of Pb at t2 is difficult to quantify directly, given the differences in matrix Pb concentrations for large vs. infinite partitioning are expected to be subtle in the present data; however, the large relative concentration of Pb between matrix and clusters supports this assumption and differences in theoretical and calculates ages based on incomplete partitioning of Pb is expected to be small for the cluster volume fraction in the BT5-13 zircon [Blum et al., in prep.]. The two 100% concordant SIMS U-Pb analyses for the BT5-13 core, and an imprecise but statistical match between <sup>207</sup>Pb/<sup>206</sup>Pb ratios derived from bulk APT data sets and SIMS, are consistent with a 3.775 Ga crystallization age and subsequent closed system U-Pb behavior on the micron scale. Using these assumptions, we can solve numerically for  $t_2$  and a model cluster age for each of the cluster definitions (Fig. 12, and Table 3); these ages vary between 2.76 to 2.80 Ga. These model cluster ages are consistent with clustering of radiogenic Pb during high temperature event(s) within the Beartooth Mountains. The estimated ages for granulite facies metamorphism (~3.25-3.1 Ga) and retrograde amphibolite facies metamorphism are within uncertainty of the calculated ages; however, the 2.76-2.8 Ga age range coincides particularly well with the intrusion of the Long Lake igneous complex at ~2.74-2.79 Ga [Mueller et al., 1988]. Independent of the exact event leading to cluster formation, these cluster model ages are yet another example of where Pb mobility and clustering (1) is temporally associated to high temperature periods in a zircon's history, and (2) the nanoscale domains are stabilized and preserved through geologic time. Understanding uncertainties surrounding measurement of isotope ratios within nanoscale domains allows for more robust evaluation of the timing and genesis of these nanoscale domains within zircon.

#### **4 Conclusions**

The ranging approaches presented here are a systematic means to assess the uncertainties associated with measurement of <sup>207</sup>Pb/<sup>206</sup>Pb ratios in nanoscale zircon domains by APT. For the BT5-13 cluster data sets, statistical and fit based approaches to placement of range bounds can provide accurate and precise Pb isotope ratios, where the precision in <sup>207</sup>Pb/<sup>206</sup>Pb ratio is limited primarily by counting statistics. At lower signal-to-noise, such as in bulk zircon data sets, these procedures are less successful and the high background results in lower signal peaks (i.e. <sup>207</sup>Pb<sup>2+</sup> at 103.5 Da) being systematically under-ranged. In such situations, accuracy is improved by

"manual" ranging, though caution is advised in assigning geological significance to these results without considering the source and magnitude of variability due to ranging and bin width. The ability to place errors on the <sup>207</sup>Pb/<sup>206</sup>Pb ratios measured in APT provides an objective means to evaluate the significance of different ratios within different domains. The signal levels, and spatial distribution of Pb within zircon BT5-13 APT data sets result in very consistent <sup>207</sup>Pb/<sup>206</sup>Pb ratios for the consistent application of several cluster identification algorithms. The ratios and uncertainties for <sup>207</sup>Pb/<sup>206</sup>Pb from SIMS, and bulk vs. clustered domains by APT support that clustered domains represent ancient reorganization of radiogenic Pb, and thus modeling of ratios may be used to estimate the timing of cluster formation. Model cluster ages of 2.8 Ga correlate with both granulite facies and amphibolite facies metamorphism within the Beartooth Mountains, as well as the intrusion of the Long Lake igneous complex. These results relate cluster formation to high-T periods within the history of BT5-13. The spatial, spectral and age data presented here highlight the potential for understanding the timing and driving forces for element reorganization as a function of time and temperature through the correlative application of APT, EBSD, and SIMS.

### Acknowledgments

We thank the Beijing CAGS SHRIMP Lab, and particularly D. Liu and A. Cavosie for their help in SIMS data collection and analysis. This research was funded by the US National Science Foundation (EAR-1144454, EAR-1524336), and the US Department of Energy, Office of Science, Office of Basic Energy Sciences, Chemical Sciences, Geosciences and Biosciences Division under award number DE-FG02-93ER14389. WiscSIMS is partly supported by the U.S. National Science Foundation (EAR-1355590). The authors acknowledge the use of facilities supported by the University of Wisconsin, College of Engineering and the Materials Research and Engineering Center (NSF DMR-121288) and Nanoscale Science and Engineering Center (NSF DMR-0832760).

## References

- Bachhav, M.N., Danoix, R., Vurpillot, F., Hannoyer, B., Ogale, S.B., Danoix, F. (2011) Evidence of lateral heat transfer during laser assisted atom probe tomography analysis of large band gap materials, Applied Physics Letters, 99, 084101.
- Blum, T.B., Darling, J.R., Kelly, T.F., Larson, D.J., Moser, D.E., Perez-Huerta, A., Prosa, T.J., Reddy, S.M., Reinhard, D.A., Saxey, D.W., Ulfig, R.M., Valley, J.W. (this volume) Best Practices for Reporting Atom Probe Analysis of Geological Materials.
- Blum, T. B., J. R. Darling, T. F. Kelly, D. J. Larson, D. E. Moser, A. Perez-Huerta, T. J. Prosa, S. M. Reddy, D. A. Reinhard, D. W. Saxey, R. M. Ulfig, and J. W. Valley (2018), Best practices for reporting atom probe analysis of geological materials, in Microstructural

- Geochronology: Planetary Records Down to Atom Scale, edited by D. Moser, F. Corfu, S. Reddy, J. Darling, and K. Tait, John Wiley & Sons, Inc., Hoboken, NJ, 232, 369-373.
- Bowring, S.A., Schmitz, M.D. (2003) High-precision U-Pb zircon geochronology and the stratigraphic record, Rev. in Min. and Geochem., 53, 305-326.
- Bunton, J.H., Olson, J.D., Lenz, D.R., Kelly, T.F. (2007) Advances in Pulsed-Laser Atom Probe: Instrument and Specimen Design for Optimum Performance, Microscopy and Microanalysis, 13, 418-427.
- Cavosie, A.J., Valley, J.W., Wilde, S.A., E.I.M.F. (2006) Correlated microanalysis of zircon: Trace element,  $\delta^{18}$ O, and U-Th-Pb isotopic constraints on the igneous origin of complex >3900 Ma detrital grains, Geochimica et Cosmochimica Acta, 70, 5601-5616.
- Chen, Y., Chou, P.H., Marquis, E.A. (2014) Quantitative atom probe tomography characterization of microstructures in a proton irradiated 304 stainless steel, Journal of Nuclear Materials, 451, 130-136.
- Cherniak, D.J., Lanford, W.A., Ryerson, F.J. (1991) Lead diffusion in apatite and zircon using ion implantation and Rutherford Backscattering techniques, *Geochimica et Cosmochimica Acta*, 55, 1663-1673.

- Cherniak, D.J., Watson, E.B. (2003) Diffusion in zircon, Rev. in Min. and Geochem., 53, 113-143.
- Currie, L.A. (1968) Limits for Qualitative Detection and Quantitative Determination: Application to Radiochemistry, Analytical Chemistry, 40(3), 586-59.
- Ewing, R.C., Meldrum, A., Wang, L., Weber, W.J., Corrales, L.R. (2003) Radiation effects in zircon, Rev. in Min. and Geochem., 53, 387-425.
- Fedo, C.M., Sircombe, K.N., Rainbird, R.H. (2003) Detrital zircon analysis in the sedimentary record, Rev.in Min. and Geochem., 53, 277-303.
- Gault, B., Moody, M.P., Cairney, J.M., Ringer, S. (2012) Atom Probe Microscopy, 396 p. Springer.
- Gedcke, D.A. (2001) How counting statistics control detection limits and peak precision. ORTEC Application Note AN59.
- Henry, D.J, Mueller, P.A., Wooden, J.L., Warner, J.L., Lee-Berman, R. (1984) Granulite grade supracrustal assemblages of the Quad Creek area, eastern Beartooth Mountains, Montana, Montana Bureau of Mines and Geology Special Publication, 84, 147-156.
- Hudson, D., Smith, G.D.W., Gault, B. (2011) Optimisation of mass ranging for atom probe microanalysis and application to the corrosion process in Zr alloys, Ultramicroscopy, 111, 480-486.
- Kirchhofer, R., Teague M.C., Gorman, B.P. (2013) Thermal effects on mass and spatial resolution during laser pulse atom probe tomography of cerium oxide, Journal of Nuclear Materials, 436, 23-28.
- Kellogg, G.L., Tsong, T.T. (1980) Pulsed-laser atom-probe field-ion microscopy, Journal of Applied Physics, 51, 1184-1192.
- Larson, D.L., Prosa, T.J., Ulfig, R.M., Geiser, B.P., Kelly, T.F., (2013) Local Electrode Atom Probe: A User's Guide. 318 p. Springer.
- Mueller, P.A., Shuster, R.D., Graves, M.A., Wooden, J.L., Bowes, D.R. (1988) Age and Complexation of a Later Archean Magmatic Complex, Beartooth Mountains, Montana-Wyoming, Montana Bureau of Mines and Geology Special Publication, 96, 7-22
- Mueller, P.A., Wooden, J.L., Nutman, A.P. (1992) 3.96 Ga Zircons from an Archean quartzite, Beartooth Mountains, Montana, Geology, 20, 327-330.
- Nasdala, L., Wenzel, M., Vavra, G., Irmer, G., Wenzel, T., Kober, B. (2001) Metamictization of natural zircon: accumulation versus thermal annealing of radioactivity-induced damage, Contributions to Mineralogy and Petrology, 141, 125-144.

- Nemchin, A., Timms, N., Pidgeon, R., Geisler, T., Reddy, S., Meyer, C. (2009) Timing of crystallization of the lunar magma ocean constrained by the oldest zircon, *Nature Geoscience*, 2, 133-136.
- Oberdorfer, C., Stender, P., Rinke, C., Schmitz, G. (2007) Laser-Assisted Atom Probe Tomography of Oxide Materials, Microscopy and Microanalysis, 13, 342-346.
- Oltman, E., Ulfig R.M., Larson, D.J. (2009) Background Removal Methods Applied to Atom Probe Data, Microscopy and Microanalysis, 15(S2), 256-257.
- Peterman, E.M., Reddy, S.M., Saxey, D.W., Snoeyenbos, D.R., Rickard, W.D.A., Fougerouse, E.M., Kylander-Clark A.R.C., (2016) Nanogeochronology of discordant zircon measured by atom probe microscopy of Pb-enriched dislocation loops, Science Advances, 2, e1601318.
- Piazolo, S., La Fontaine, A., Trimby, P., Harley, S., Yang, L., Armstrong, R., Cairney, J.M. (2016) Deformation-induced trace element redistribution in zircon revealed using atom probe tomography, Nature Communications, 7, 10490.
- Reddy, S.M., van Riessen, A., Saxey, D.W., Johnson, T.E., Rickard, W.D.A., Fougerouse, D., Fischer, S., Prosa, T.J., Rice, K.P., Reinhard, D.A., Chen, Y., Olson, D. (2016) Mechanisms of deformation-induced trace element migration in zircon resolved by atom probe and correlative microscopy, Geochimica et Cosmochimica Acta, 195, 158-170.
- Reinhard, D.A., Moser, D.E., Barker, I.R., Olson, D., Martin, I., Rice, K.P., Chen, Y., Lawrence, D., Prosa, T.J., Larson, D.J., (2015) Atom Probe Tomography of Zircon and Baddeleyite Geochronology Standards, Microscopy and Microanalysis, 21(3), 0426.
- Schoene, B., Schaltegger, U., Brack, P., Latkoczy, C., Stracke, A., Günther, D. (2012) Rates of magma differentiation and emplacement in a ballooning pluton recorded by U-Pb TIMS-TEA, Adamello batholith, Italy, Earth and Planetary Science Letters, 355-356, 162-173.
- Valley, J.W. (2003) Oxygen isotopes in zircon, Reviews in Mineralogy and Geochemistry, 53, 343-385.
- Valley, J.W., Lackey, J.S., Cavosie, A.J., Clechenko, C.C., Spicuzza, M.J., Basei, A.S., Bindeman, I.N., Ferreira, V.P., Sial, A.N., King, E.M., and others, (2005) 4.4 billion years of crustal maturation: oxygen isotope ratios of magmatic zircon, Contributions to Mineralogy and Petrology, 150, 561-580.
- Valley J.W., Cavosie, A.J., Ushikubo, T., Reinhard, D.A., Lawrence, D.F., Larson, D.J., Clifton, P.H., Kelly, T.F., Wilde, S.A., Moser, D.E., Spicuzza, M.J. (2014a) Hadean age for post-

- magma-ocean zircon confirmed by atom probe tomography, Nature Geoscience, 7, 219-223.
- Valley, J.W., Spicuzza, M.J., Ushikubo, T. (2014b) Correlated  $\delta^{18}O$  and [Ti] in lunar zircons: a terrestrial perspective for magma temperatures and water content on the Moon, Contributions to Mineralogy and Petrology, 167, 956.
- Valley, J.V. Reinhard, D.A., Cavosie, A.J., Ushikubo, T., Lawrence, D.F., Larson, D.J., Kelly, T.F., Snoeyenbos, D.R., Strickland, A. (2015) Nano- and Micro-geochronology in Hadean and Archean zircons by atom-probe tomography and SIMS: New tools for old minerals, American Mineralogist, 100, 1355-1377.
- Vella, A., Mazumder, G., Da Costa, G., Deconihout, B., (2011) Field evaporation mechanism of bulk oxides under ultra fast laser illumination, Journal of Applied Physics, 110:044321.
- Vurpillot, F., Larson, D.J., Cerezo, A. (2004) Improvement of multilayer analyses with a three-dimensional atom probe, Surface and Interface Analysis, 36, 552-558.

- **Figure 1**. (a) Backscatter electron (BSE) image of zircon BT5-13. Lift-out location indicated with red outline indicating cuts, and solid region indicating the wedge used to generate APT specimens. Small fractures shown with white arrows. (b) Cathodoluminescence (CL) image of BT5-13 showing location of SIMS U-Pb age analyses. (c) Concordia showing the two U-Pb age analyses for BT5-13. (d) Relative misorientation map (units of degrees). Reference orientation is the mean orientation of the grain. (e) Band contrast map. (f) inverse pole figure orientation map. (g) Pole figures for BT5-13. Note: grain maps (d-f) and pole figures are the same orientation.
- **Figure 2**. Atom probe mass spectra for BT5-13 zircon data sets; showing major and selected trace element peaks/peak families. Note: colored regions are schematic identifiers, and do not equate to range bounds used in analysis. Bin width is set to 0.020 Da for all spectra. (a) Mass spectrum for specimen M1\_491. Note spectrum cutoff at 200 Da. (b) Mass spectrum for specimen M5\_568. Spectrum cutoff at 400 Da. (c) Mass spectrum for specimen M3\_609. Spectrum cutoff at 400 Da. (d) Expanded section of M3\_609 mass spectrum between 0 and 130 Da showing major peak families.
- **Figure 3**. Pb atom maps for M5\_491, M3\_609, and M1\_568. Expanded views are 25x25x25 nm cubes highlighting cluster morphology and are oriented to show high density layering at the upper surface of clusters. Only Pb ions are shown, however all ions, not only Pb, are co-localized within high density layers.
- **Figure 4.**  $\kappa$ th nearest neighbor distributions for order,  $\kappa$ , 1 through 10, completed on 250 nm segments of the (a) M5\_491, (b) M5\_568, and (c) M3\_609 data sets. The distributions from the BT5-13 data sets are shown (left), along with the expected distribution if Pb were randomly distributed (right). Distributions represent the number of occurrences of a given Pb-Pb spacing between the  $\kappa$ th nearest Pb atom. The rightmost peak at any given  $\kappa$  is associated with the distribution of distances for widely spaced matrix Pb. At shorter d, there exists a peak for clustered Pb (which possesses shorter inter-Pb distances relative to the matrix) and a peak at small d which is an artifact of the high density layering within the reconstruction (see Fig. 3). For  $\kappa$ NN analysis, the maximum separation parameter input is taken as the minimum between the matrix and clustered distributions. Randomized distributions represent ion positions and bulk compositions identical to the input data, but with the random assignment of ion identity (see *Larson et al.*, [2013]). Prders 2 through 5 (filled surface) are the order parameters used during  $\kappa$ NN cluster characterization (see Fig. 7-9).
- Figure 5. Schematic representation of the ranging methodology based on comparing counts within a single bin,  $C_i$ , to a statistical cutoff, taken here as either the critical limit for counts within a single bin ( $L_C$ ) or as the detection limit for counts within a single bin ( $L_D$ ) (both  $L_C$  and  $L_D$  are calculated based on a confidence level of 95%: see text for details). (a) Approximate locations of backgrounds  $B_1$ , and the associated  $C_1$ = $L_C$  cutoff level used in defining range bounds. Detailed position of bins shifts slightly based on binning of data. (b) Systematic comparison of counts in the *i*th bin  $C_1$ , and adjacent bins to establish range bounds. (c) Final range bounds, with range widths equal to  $^{206}$ η<sub>1</sub> and  $^{207}$ η<sub>1</sub>. (d) Estimation of uncertainty in  $^{207}$ Pb/ $^{206}$ Pb due to ranging, where  $\sim$ 25% of the  $^{206}$ η<sub>1</sub> and  $^{207}$ η<sub>1</sub> are added to each side of the initial ranges. In the case shown, the region between  $^{206}$ η<sub>1</sub> and  $^{207}$ η<sub>1</sub> is less than ( $^{206}$ η<sub>1</sub>+ $^{207}$ η<sub>1</sub>)/4 and thus counts between  $^{206}$ η<sub>1</sub> and  $^{207}$ η<sub>1</sub> are divided equally in calculation of ( $^{207}$ Pb/ $^{206}$ Pb)<sub>η2</sub>.
- **Figure 6**. Schematic representation of ranging based on fitting of peak tails. Starting spectrum shown in (a). Peak fitting and determination of range bounds is approached using an iterative background stripping scheme; the background corrected fit to the 103.0 Da peak tail (b) is used to correct the 103.5 Da peak for <sup>206</sup>Pb, and the tail of the 103.5 Da peak is then fit (c). The fits to the corrected spectra are used to establish integration bounds within the peak tails by establishing when the fit drops below the critical limit, L<sub>C</sub>. The low-side integration bounds of each peak are placed analogous to above, accounting for the additional "background" counts present under the 103.5 Da peak. (See text for details).
- **Figure 7.** Results for cluster analyses showing atoms of Pb in specimen M5\_491 (left) and clusters identified within the  $\kappa$ th order Nearest Neighbor cluster analysis (i.e.  $\kappa$ CA) and the 0.25% and 0.5% atomic Pb isoconcentration surfaces. All ions shown in the identified clusters. n refers to the number of distinct clusters.
- **Figure 8**. Results for cluster analyses showing atoms of Pb in specimen M1\_568 (left) and clusters identified within the  $\kappa$ th order Nearest Neighbor cluster analysis (i.e.  $\kappa$ CA) and the 0.25% and 0.5% atomic Pb isoconcentration surfaces. All ions shown in the identified clusters. n refers to the number of distinct clusters.

**Figure 9.** Results for cluster analyses showing atoms of Pb in specimen M3\_609 (left) and clusters identified within the  $\kappa$ th order Nearest Neighbor cluster analysis (i.e.  $\kappa$ CA) and the 0.25% and 0.5% atomic Pb isoconcentration surfaces. All ions shown in the identified clusters. n refers to the number of distinct clusters.

**Figure 10**. Summary of ranging and uncertainty analysis for the concatenated 0.5% atomic Pb clusters, (Fig. 7-9). (a-c) Total counts, background and signal levels for  $^{206}\text{Pb}$  and  $^{207}\text{Pb}$  using the ranging procedure outlined in Figs. 5 and 6; (a) ranging based on  $L_C$ , (b) ranging based on  $L_D$  and (c) ranging based on fitting of peak tails. Error bars are  $2(T^{1/2})$  for reference. (d-f) calculated  $^{207}\text{Pb}/^{206}\text{Pb}$  ratios as a function of bin width, for ranging procedures outlined in Figs. 5 and 6. (d) ranging based on  $L_C$ , (e) ranging based on  $L_D$  and (f) ranging based on fitting of peak tails. Filled black data points represent a range of bin widths between 0.010 and 0.045 Da over which signal levels and calculated ratios are relatively stable (see text). Red data point represents data summarized in Table 3, and quoted in text

**Figure 11** .Summary of ranging and uncertainty analysis for concatenated bulk APT data sets, using constant integration bounds at ~102.8-103.2 Da for the 103.0 peak, and ~103.4-103.6 Da for the 103.5 Da peak. Backgrounds for each peak are calculated over the regions ~102.4-102.8 Da for the 103.0 Da range, and ~103.2-103.4 Da for the 103.5 Da range. If the single range between ~102.4-102.8 Da is used to correct the 103.5 Da range, calculated <sup>207</sup>Pb signals are below zero. (a) Total counts, background and signal levels for <sup>206</sup>Pb and <sup>207</sup>Pb plotted versus bin width. Error bars are  $2(T^{1/2})$  for reference. (b) calculated <sup>207</sup>Pb/<sup>206</sup>Pb ratios as a function of bin width. Horizontal lines show the (<sup>207</sup>Pb/<sup>206</sup>Pb)\* = 0.3666 ± 0.0044 ratio measured by SIMS (black line) along with ±2 $\sigma$  (red lines). Red data point represents data summarized in Table 3 and quoted in text.

**Figure 12**.  $^{207}\text{Pb}/^{206}\text{Pb}$  isotope evolution for BT5-13 based on present day U concentrations and a crystallization age of 3.775 Ga. (a)  $^{207}\text{Pb}/^{207}\text{Pb}$  as a function of time after crystallization. The solid red vertical line represents the modeled cluster age for  $^{207}\text{Pb}/^{206}\text{Pb} = 0.723 \pm 0.061$  measured within the concatenated 0.5% atomic Pb clusters. Dashed vertical red lines show upper and lower bounds based on uncertainty in the  $^{207}\text{Pb}/^{206}\text{Pb}$  ratio.

Table 1. Summary of electron backscatter diffraction (EBSD) acquisition and analysis.

SEM Model	Hitachi S3400-N						
<b>Instrument Settings</b>							
EBSD Software	HKL Channel 5						
Conductive Coat	None						
Acc. Voltage	$20.0\mathrm{kV}$						
Working Distance	23.5mm						
Spot Size	-						
Tilt	70°						
Software and Acquisition Settings							
EBSP collection time per frame (ms)	45						
EBSP noise reduction (frames)	400						
Binning	2x2						
Gain	(high)						
Hough Resolution	70						
Band Detection (min/max)	6/7						
Mean band contrast (zircon)	139.7						
X steps	348						
Y steps	209						
Step Distance (µm)	0.5						
Average mean angular deviation	0.4434						
Noise Reduction – "wildspike"	No						
<i>n</i> neighbor zero solution extrapolation	<b>-</b>						
Kuwahara Filter	<u>-</u>						
Data Analysis Software	MATLAB: MTEX Toolbox (version 4.3.1)						

**Table 2.** Atom Probe Tomography data acquisition settings and run summary (for summary of terms, see *Blum* et al., [this volume]).

Specimen/Data Set	M5_491	M1_568	M3_609			
<b>Instrument Model</b>	LEAP 5000 XR	LEAP 5000 XR	LEAP 5000 XR			
<b>Instrument Settings</b>						
Laser Wavelength (nm)	355	355	355			
Laser Pulse Energy (pJ)	200	200	200			
Pulse Frequency (kHz)	125	125	125			
Evaporation Control	<b>Detection Rate</b>	<b>Detection Rate</b>	<b>Detection Rate</b>			
Target Detection Rate (ions/pulse)	0.01	0.01	0.01			
Nominal Flight Path (mm)	382	382	382			
Set Point Temperature (K)	50	50	50			
Sample Temperature (K)	55	55	55			
Chamber Pressure (Torr)	$1.3 \times 10^{-10}$	$1.4 \times 10^{-10}$	$5.4 \times 10^{-11}$			
Data Summary						
LAS Root Version	15.41.342j	15.41.342j	15.41.342j			
CAMECAROOT Version	15.43.393e	15.43.393e	15.43.393e			
Analysis Software	IVAS 3.6.10a	IVAS 3.6.10a	IVAS 3.6.10a			
Total Ions:	150,792,481	163,057,160	213,529,143			
Single (%)	66.1	69.2	68.1			
Multiple (%)	33.1	30.1	31.2			
Partial (%)	0.8	0.7	0.7			
Reconstructed Ions:	140,428,802	155,697,119	194,541,231			
Ranged (%)	79.4	75.2	76.7			
Unranged (%)	20.6	24.8	23.3			
Volt./Bowl Corr. Peak (Da)	16	16	16			
Mass Calib. (peaks/interp.)	10/Lin.	11/Lin.	11/Lin.			
$^{\dagger}(\mathrm{M}/\Delta\mathrm{M})$ for $^{16}\mathrm{O_2}^+$	1130	1200	1180			
$^{\dagger\dagger}({ m M}/{ m \Delta}{ m M}_{10})$	530	550	540			
time independent background	20.5	19.7	18.7			
(ppm/ns)	20.3	17.1	10.7			
Reconstruction						
Final specimen state	intact	intact	fractured			
Pre-/Post-analysis Imaging	SEM/SEM	SEM/SEM	SEM/n.a.			
Radius Evolution Model	"shank"	"shank"	"shank"			
Field Factor (k)	3.3	3.3	3.3			
Image Compression Factor	1.65	1.65	1.65			
Assumed Electric Field (V/nm)	28	28	28			
Detector Efficiency (%)	52	52	52			
Average Atomic Volume (nm <sup>3</sup> )	0.0108	0.0108	0.0108			
$V_{initial}; V_{final}(V)$	4546; 9608	4305; 10383	4848; 11719			

 $<sup>^{\</sup>dagger}\Delta M$  is full width at half maximum.

 $<sup>^{\</sup>dagger\dagger}\Delta M_{10}$  is full width at tenth maximum.

**Table 3**. Summary of SIMS U-Pb and APT Pb isotope data. Uncertainties are  $1\sigma$  unless otherwise stated.

SIMS U <sup>†</sup>	Th <sup>†</sup>	<sup>204</sup> Pb/ <sup>20</sup>	)6ph	<sup>208</sup> Pb/ <sup>206</sup>	<sup>б</sup> РЬ	<sup>207</sup> Pb*/ <sup>206</sup> Pb*	208 <sub>T</sub>	Pb*/ <sup>232</sup> Th	206 <b>p</b> l-	>*/ <sup>238</sup> U	<sup>207</sup> Pb*/ <sup>235</sup> U	Err. Corr.	<sup>207</sup> Pb*/ <sup>206</sup> P Age	b* Conc.
BT5-13-2 320	97	0.0000					.1996±0.0072 0.7945±0.027		40.16±1.365	0.987	3778±8			
BT5-13-3 325	102	0.000016		0.085±0.006		0.3652±0.0011		0.2074±0.0073		0±0.027	39.98±1.359	0.996	3772±5	
† Concentrations in μg/g * Radiogenic														
APT				Pb Counts (ions		)		=			Pb Ra	atios		
Cluster Definition	n	<sup>207</sup> T <sup>207</sup> B		<sup>207</sup> S <sup>206</sup> T <sup>206</sup> B		<sup>206</sup> S	$^{207}\sigma_{\rm S}$	<sup>206</sup> σ <sub>S</sub> σ <sub>7/6,rangin</sub>		<sup>207</sup> Pb/ <sup>206</sup> Pb	Cluster Model Ag ±2σ (Ma)			
Bulk														
APT $(L_C)$	-	12987	12170	817	37745	33468	4277	158.6	266.9	0.018	0.191	0.080	-	-
APT ("manual")	-	58882	57408	1474	12046	116289	4172	341.0	486.6	-	0.353	0.183	-	-
SIMS (BT5-13-2)	-	-	-	-	-	-	-	-	-	-	0.367	0.0037	-	-
SIMS (BT5-13-3)	-	-	-	-	-	-	-	-	-	-	0.365	0.0022	-	-
κNN (clusters)														
2CA ( <i>Lc</i> )	11	1343	18.24	1325	1862	20.06	1842	36.9	43.4	0.0019	0.719	0.053	2754	+210/-230
$2CA(L_D)$	11	1334	15.50	1319	1843	15.5	1828	36.7	43.1	0.0003	0.722	0.052	2767	+200/-230
2CA (Fit)	11	1345	24.28	1321	1871	23.33	1848	36.6	43.1	-	0.715	0.052	2738	+210/-230
3CA ( <i>Lc</i> )	11	1393	22.20	1371	1935	25.90	1909	37.6	44.3	0.0029	0.718	0.052	2750	+200/-230
$3CA(L_D)$	11	1379	17.50	1362	1904	16.62	1887	37.4	43.8	0.0022	0.722	0.052	2767	+200/-230
3CA (Fit)	11	1396	27.39	1369	1938	26.67	1911	37.3	43.9	-	0.716	0.051	2742	+200/-230
$4CA(L_C)$	10	1408	25.80	1382	1950	28.67	1921	37.9	44.5	0.0023	0.719	0.052	2754	+200/-230
$4CA(L_D)$	10	1395	21.84	1373	1920	20.16	1900	37.6	44.0	0.0018	0.723	0.052	2771	+200/-230
4CA (Fit)	10	1410	32.20	1378	1955	31.11	1924	37.1	44.1	-	0.716	0.051	2742	+200/-230
$5CA(L_C)$	10	1429	30.60	1398	1979	35.70	1943	38.2	44.9	0.0015	0.720	0.052	2759	+200/-230
5CA ( <i>L<sub>D</sub></i> )	10	1410	26.00	1384	1956	28.89	1927	37.9	44.6	0.0031	0.718	0.052	2750	+200/-230
5CA (Fit)	10	1433	39.44	1394	1987	38.11	1949	37.5	44.4	-	0.715	0.051	2738	+200/-230
Isosurface (clusters)														
0.25% atm Pb ( $L_C$ )	9	1084	39.20	1045	1471	44.8	1426	33.5	38.9	0.0001	0.733	0.061	2811	+230/-260
$0.25\%$ atm Pb $(L_D)$	9	1076	36.00	1040	1448	36.00	1412	33.3	38.5	0.0005	0.737	0.062	2827	+230/-270
0.25% atm Pb (Fit)	9	1091	51.55	1039	1477	50.4	1427	32.9	38.5	-	0.728	0.061	2791	+230/-270
0.5% atm Pb ( $L_C$ )	6	1041	28.20	1013	1429	31.33	1398	32.7	38.2	0.0004	0.725	0.061	2771	+230/-270
$0.5\%$ atm Pb $(L_D)$	6	1028	24.00	1004	1406	24.00	1382	32.4	37.8	0.0023	0.727	0.061	3016	+250/-290
0.5% atm Pb (Fit)	6	1041	30.68	1010	1427	30.00	1397	32.0	37.7	-	0.723	0.061	2771	+230/-270
Single Cluster $(L_C)$	1	215	8.00	207	271	8.00	263	14.9	16.7	0.0017	0.787	0.152	3016	+470/-650
Single Cluster $(L_D)$	1	184	3.50	181	256	5.06	251	13.7	16.2	0.0190	0.721	0.149	2763	+530/-750

215

7.40

208

269

7.30

262

14.4

0.152

+470/-640

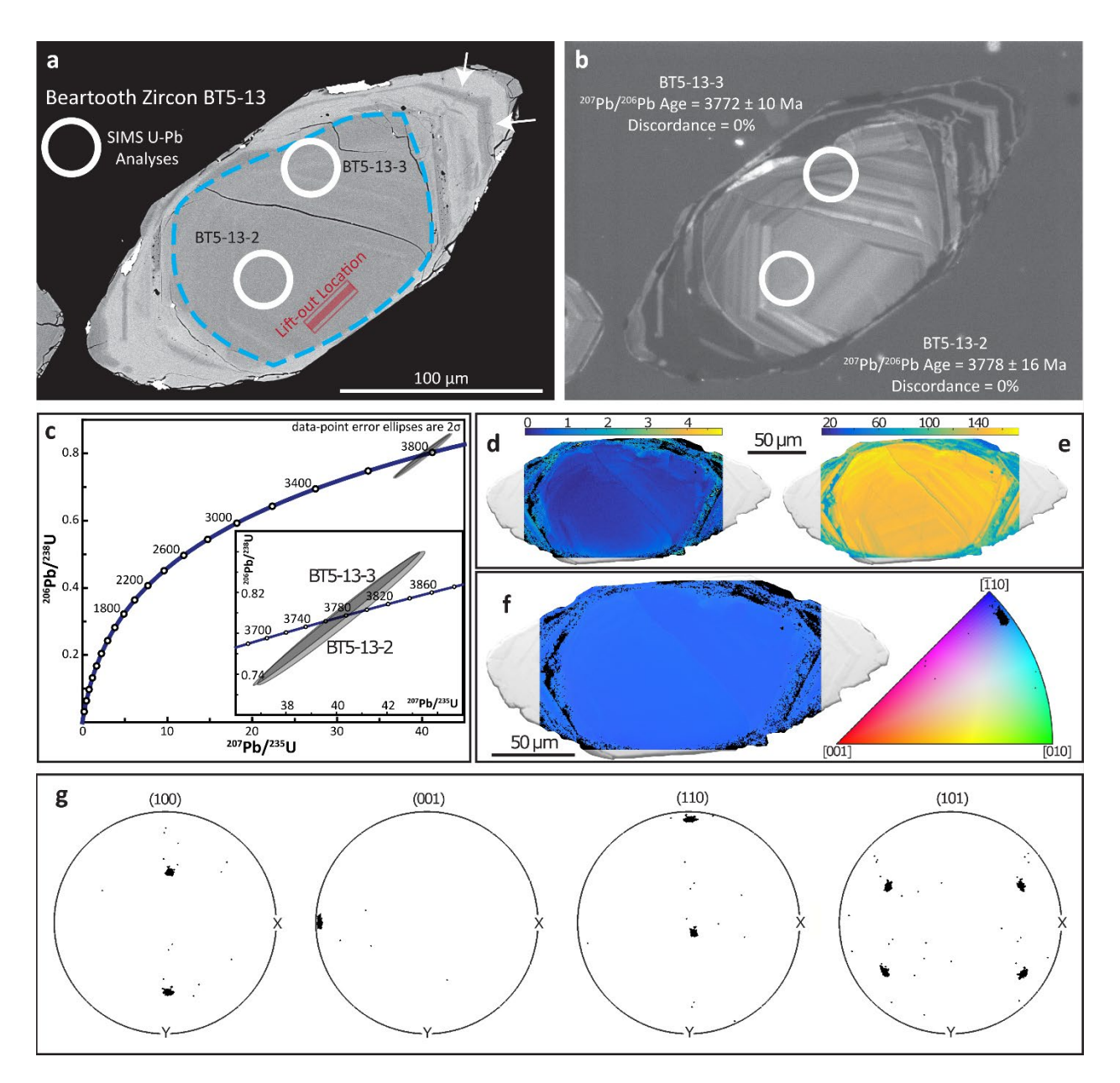


Figure 1

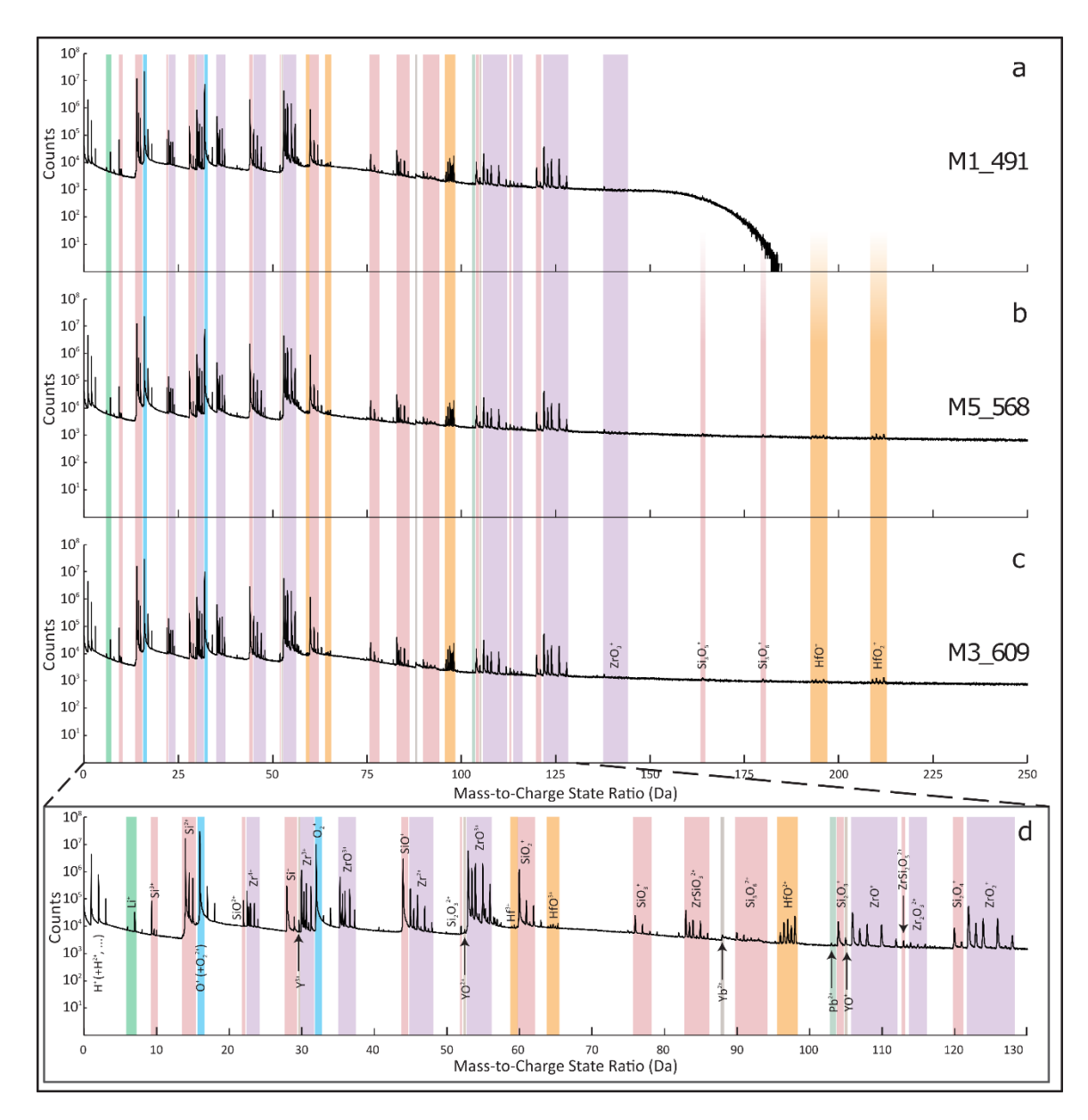


Figure 2

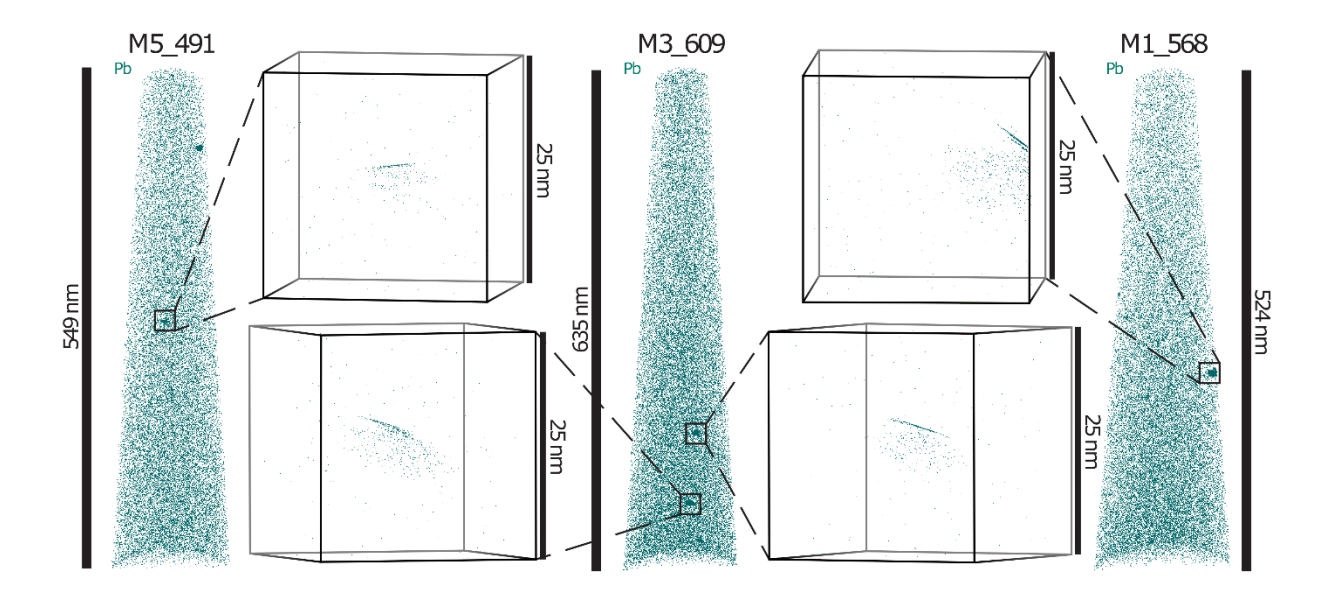


Figure 3

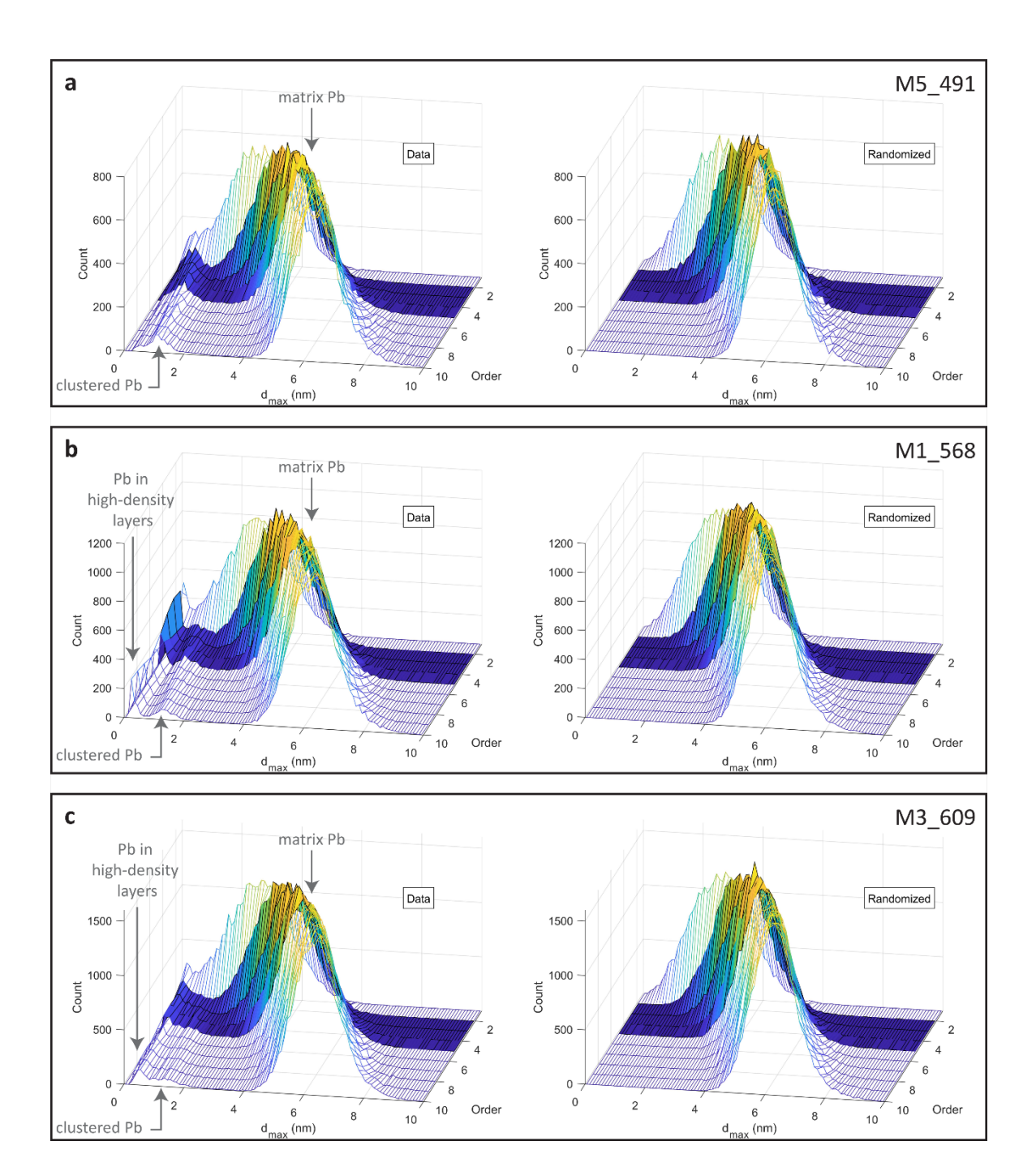


Figure 4

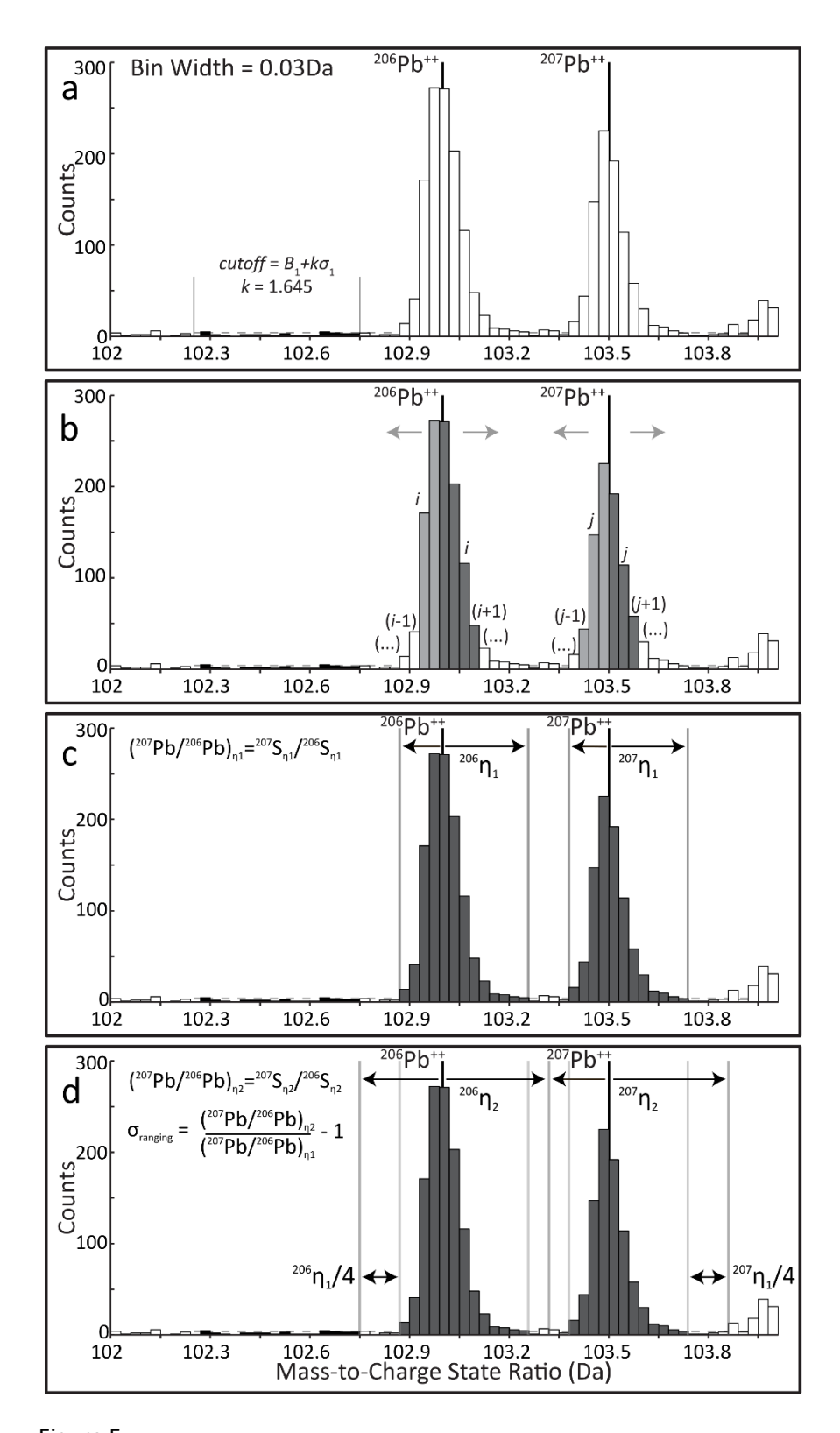


Figure 5

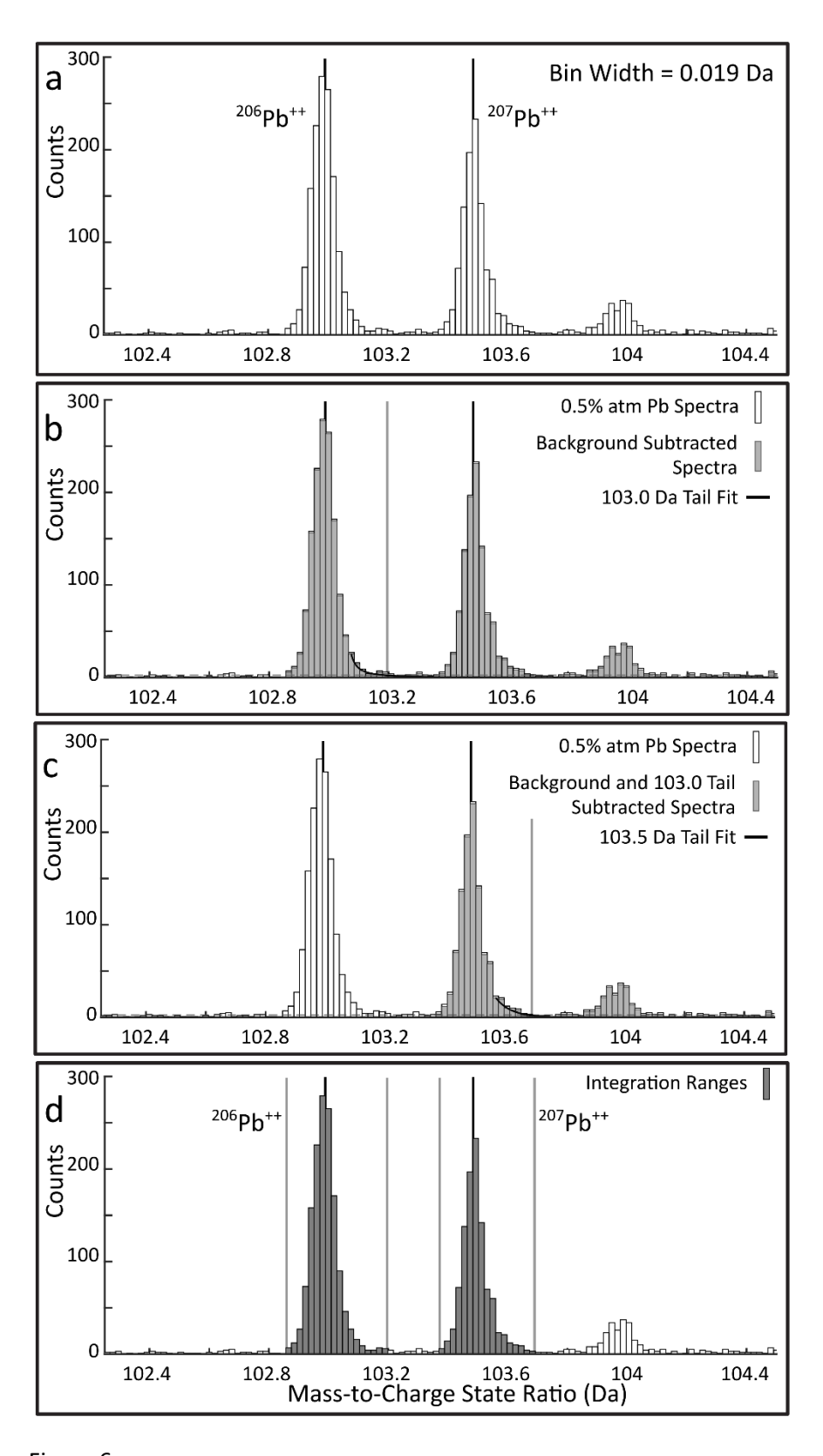


Figure 6

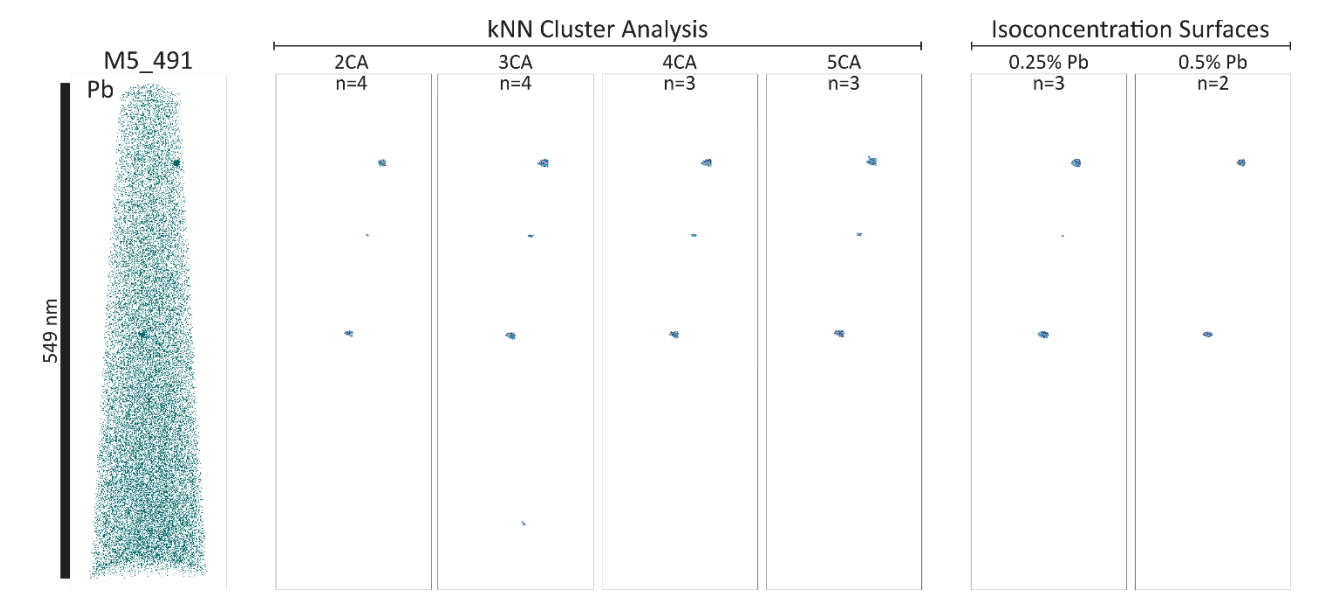


Figure 7

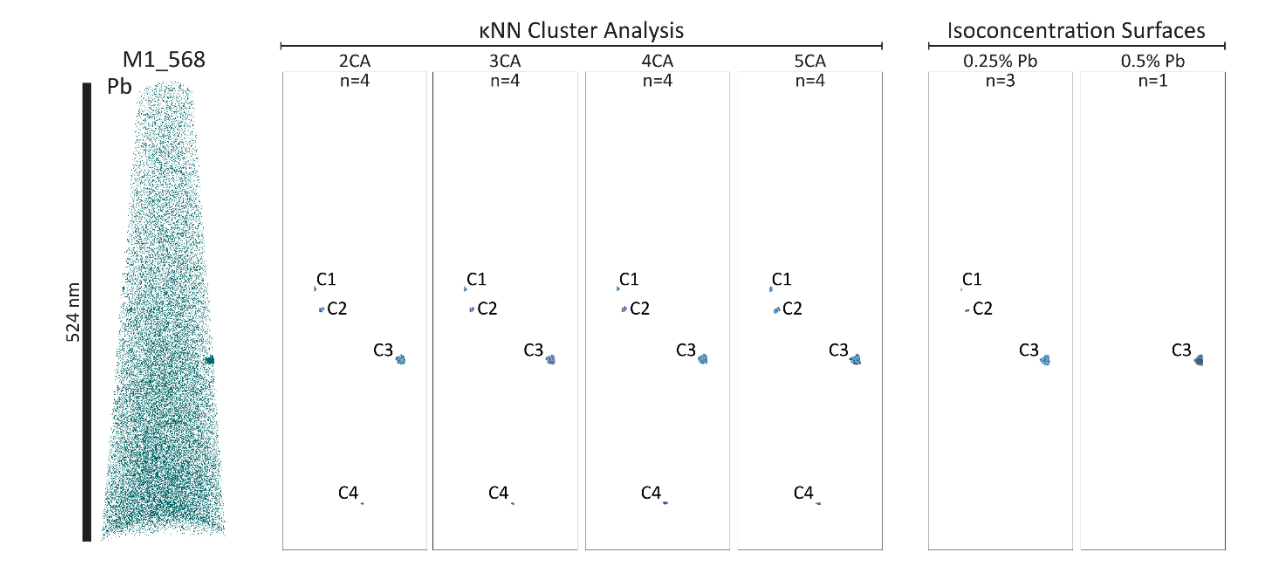


Figure 8

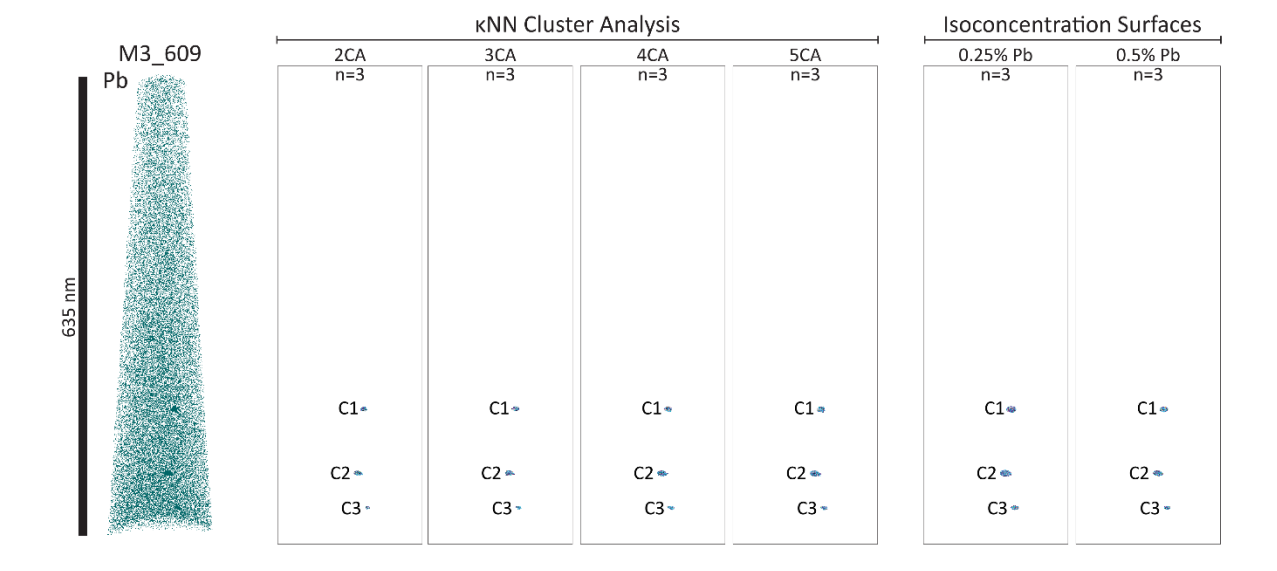


Figure 9

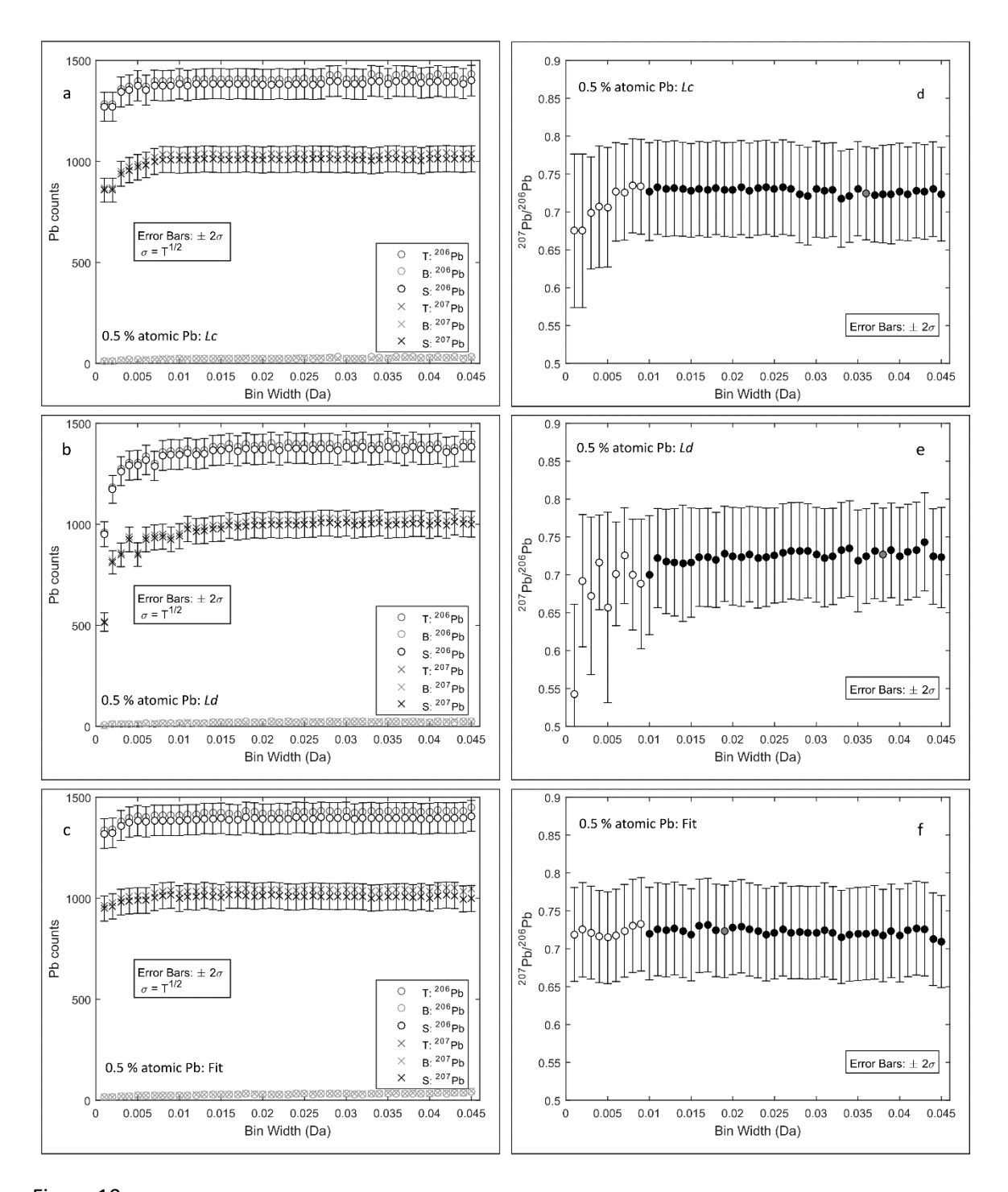
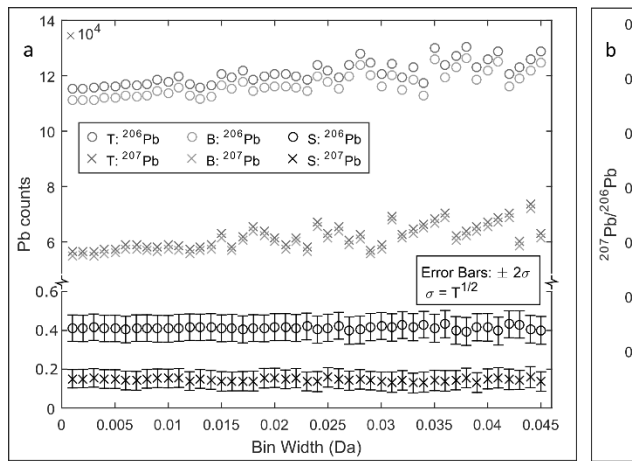


Figure 10



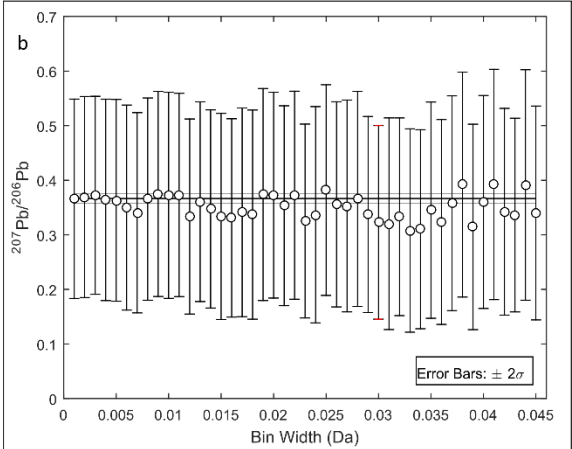


Figure 11

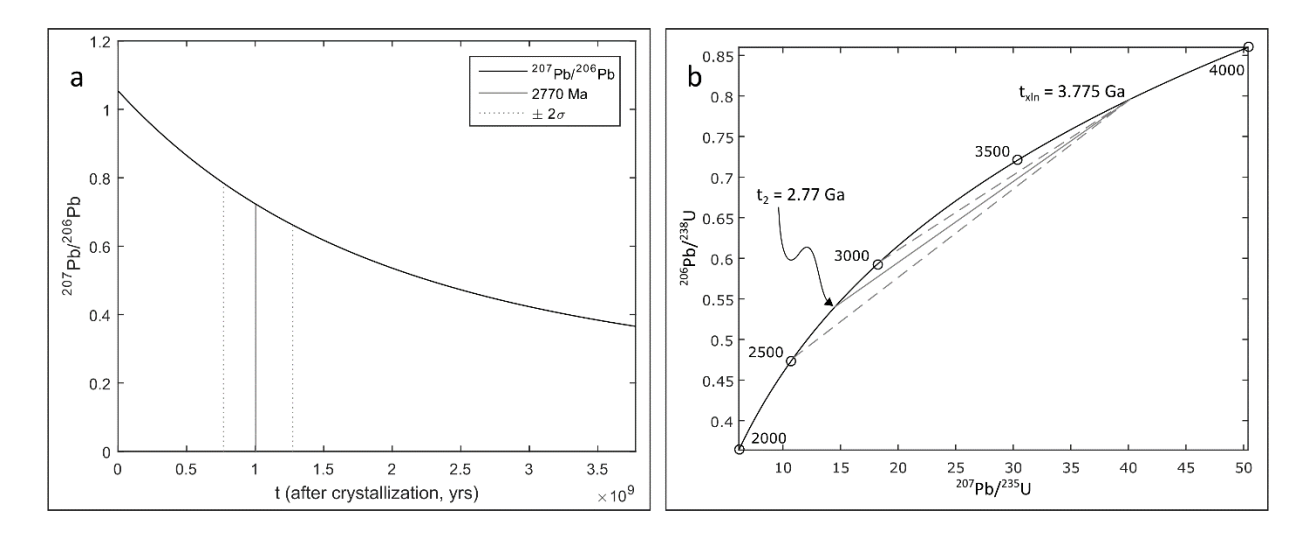


Figure 12